# Cell cycle-dependent mRNA localization in P-bodies

Adham Safieddine[1,*], Marie-Noëlle Benassy[1], Thomas Bonte[2], Floric Slimani[3], Oriane Pourcelot[3], Michel Kress[1], Michèle Ernoult-Lange[1], Maïté Courel[1], Emeline Coleno[3], Arthur Imbert[2], Antoine Laine[4], Annie Munier Godebert[5], Angelique Vinit[5], Corinne Blugeon[6], Guillaume Chevreux[7], Daniel Gautheret[4], Thomas Walter[2], Edouard Bertrand[3], Marianne Bénard[1], Dominique Weil[1,*]

1: Sorbonne Université, CNRS, Institut de Biologie Paris Seine (IBPS), Laboratoire de Biologie du Développement, France

2 : Centre for Computational Biology (CBIO), Mines Paris, PSL University, Paris, France

3 : Institut de Génétique Humaine, University of Montpellier, CNRS, Montpellier, France

4 : Institute for Integrative Biology of the Cell, UMR 9198, CEA, CNRS, Université Paris-Saclay, Gif-Sur-Yvette, France

5: Sorbonne University, CISA flow cytometry facility, Research Center Saint-Antoine (CRSA), UMRS 938, F-75012 Paris, France.

6: Génomique ENS, Institut de Biologie de l'ENS (IBENS), Département de biologie, École normale supérieure, CNRS, INSERM, Université PSL, 75005 Paris, France

7: Université Paris Cité, CNRS, Institut Jacques Monod, 75013 Paris, France.

*Correspondence: dominique.weil@upmc.fr (D.W), adham.safieddine@sorbonne-universite.fr (A.S)

**Abstract:**

Understanding the dynamics of RNA targeting to membraneless organelles is essential to disentangle their functions. Here, we investigate how P-bodies (PBs) evolve during cell cycle progression. PB purification at different cell cycle phases uncovers widespread changes in their RNA content. Importantly, these changes are partly uncoupled from cell cycle-dependent changes in RNA expression. Single molecule FISH shows various mRNA localization patterns in PBs peaking in G1, S, or G2, with multiple examples illustrating the timely capture of mRNAs in PBs when their encoded protein becomes dispensable. Cyclic mRNA localization in PBs does not directly reflect their non-polysomal pool. While mRNA localization in PBs is tightly linked to their GC content at all cell cycle phases, PB mRNAs are specifically longer in G1. Altogether, our study supports a model where PBs are more than a default location for excess untranslated mRNAs and suggests an RNA-mediated seeding mechanism for post-mitotic PB reassembly.

**Keywords:**

P-bodies, RNA localization, RNA imaging, cell cycle

**Highlights:**

- The RNA content of PBs is dynamics during cell cycle progression
- Cyclic mRNA accumulation in PBs is in part uncoupled from mRNA expression in the cytoplasm
- smFISH highlights various patterns of cyclic mRNA accumulation in PBs, particularly in G1
- PBs do not buffer excess non-polysomal mRNAs
- PB mRNAs have particularly long CDSs in G1 but not G2, while they are strikingly AU-rich all along the cell cycle

## Introduction

Proper compartmentalization of biological molecules is a fundamental aspect of cellular organization. In the last decade, membraneless organelles received increasing attention and appreciation for their contribution in organizing subcellular space[1–5]. In eukaryotic cells, many such organelles have been identified both in the nucleus, including for instance nucleoli, Cajal bodies, speckles and paraspeckles, and in the cytoplasm, including stress granules and P-bodies (PBs).

PBs are ribonucleoprotein granules (RNPs) widespread throughout eukaryotes and constitutively present in mammalian cells[6]. They contain a large variety of RNA binding proteins involved in translation regulation and RNA decay. Our previous purification of PBs from asynchronous human cells allowed the characterization of their RNA content[7]. PBs accumulate a large variety of RNAs, corresponding to one third of the coding transcriptome. These mRNAs are generally abundant, but inefficiently translated. Furthermore, PB mRNAs are strikingly AU-rich[8]. This nucleotide bias in the coding sequence (CDS) results in a codon usage strongly biased towards low usage codons, which leads to poor protein yield. In addition, their AU-rich 3' untranslated regions (3'UTRs) favors their accumulation in RNP granules, likely due to preferential binding to condensation-prone RNA-binding proteins (RBPs). In terms of cellular functions, PB-enriched mRNAs tend to encode regulatory proteins whereas the mRNAs encoding house-keeping proteins tend to be excluded from PBs[7]. While these studies provided a first genome-wide picture of the PB transcriptome, further studies are required to understand to which extent PBs adapt their content to cellular needs.

Various approaches have been used to investigate RNA localization in PBs. In situ hybridization first showed that mRNA repressed by miRNA localize to PBs[9]. Then, single molecule tracking of microinjected RNAs allowed examining their trafficking at a high temporal resolution over minutes[10]. This revealed that miRNAs, repressed mRNAs, and lncRNAs can associate transiently or stably with PBs, in part depending on their functionality. Other studies addressed RNA localization in PBs in response to translational stress. For instance, relief of miR122-mediated silencing in response to amino acid starvation or oxidative stress causes the release of its CAT-1 mRNA target from PBs[11]. A prolonged amino acid starvation, that leads to 60% translation reduction, also increased exogenous RNA targeting to PBs[12]. While such studies suggested a regulatory potential of mRNA targeting to PBs under condition of extreme translational reprogramming, the dynamics of the PB transcriptome in unstressed conditions have not been investigated.

77 The cell cycle is a program of physiological and molecular changes a cell undergoes to
78 produce two daughter cells. From an RNA metabolism perspective, cell cycle progression is well
79 characterized, with specific waves of transcription[13–18] and RNA degradation[19–23]. In terms of
80 translation, a previous study highlighted that proliferative cells have a distinct tRNA signature
81 compared to differentiating or arrested cells, which may favor the translation of mRNAs with AU-
82 rich codon usage[24]. Regarding PBs, it was shown that they dissolve at every mitosis, reform in
83 G1 phase, and enlarge during S phase progression[25]. Interestingly, we previosuly found that,
84 among the various regulatory proteins encoded by PB mRNAs, cell cycle regulators were
85 particularly enriched[6,7]. For these reasons, we chose to investigate the dynamics of RNA
86 localization in PBs in the context of the cell cycle.

87 Here, we first determined the composition of PBs purified at various cell cycle stages. This
88 revealed widespread changes in the RNA content of PBs during cell cycle progression. Some of
89 these changes were uncoupled from those occurring in the cytoplasm (the ones resulting from
90 variations in mRNA transcription or stability), demonstrating a regulatory potential of PBs. Single
91 molecule FISH (smFISH) confirmed the diversity of PB localization patterns, with maximal
92 localization in PBs peaking in G1, S or G2 phase, depending on the transcript. Notably, some
93 mRNAs particularly expressed in G2 traffic to PBs specifically in early G1, at a time where their
94 encoded protein is no longer needed. Reporter mRNAs and puromycin experiments show that
95 the cyclic pattern of PB localization is not directly related to the amount of untranslated transcripts
96 in the cytoplasm. While we did not find any phase-specific nucleotide or codon usage bias, we
97 observed a G1 phase-specific contribution of CDS length. Altogether, our results demonstrate the
98 existence of differential RNA localization in PBs operating across the cell cycle and suggest that
99 RNAs with long CDSs are central to the formation of new PBs in early G1.

## Results

### PBs enlarge during cell cycle progression

Before analyzing the content of the PBs during the cell cycle, we first refined the description of their global morphology and number across the cell cycle. To identify cell cycle stages, we relied on the PIP-FUCCI system. PIP-FUCCI allows accurate determination of cell cycle phases by expressing decay-sensitive fragments of two known cyclic proteins fused to fluorescent markers: (i) $Cdt_{11–17}$-mVenus expressed in G1, G2 and mitosis (G2/M); and (ii) mCherry-$Gem_{1-110}$ expressed in S and G2/M phases[26,27]. Both markers are fused with nuclear localization elements to make them compatible with cytoplasmic co-labeling. The accurate cell cycle-dependent expression of PIP-FUCCI was verified by flow cytometry analysis of live cells after DNA labeling with Hoechst. The mVenus positive, mCherry positive, and double positive cells showed the expected quantity of DNA (1N to 2N) for cells in G1, S, and G2/M phases, respectively (Figure S1A, B). PB labeling by immunofluorescence (IF) against the classical PB marker DDX6 (Figure 1A) showed that PB size increased from G1 to G2 (Figure S1C), and DDX6 mean intensity in PBs increased in G2 (Figure S1D) regardless of PB size (Figure 1B). However, the number of PBs per cell increased only modestly (Figure S1E). To investigate if these changes resulted from increased expression of PB proteins required for (DDX6, LSM14A and 4E-T) or contributing to (PAT1B) human PB assembly[28], we separated HEK293-FUCCI cells in G1, S and G2/M phases using fluorescence activated cell sorting (FACS). However, none of the tested proteins was induced across the cell cycle (Figure S1F). In summary, after dissolving in mitosis, PBs form in G1, progressively enlarge during interphase, particularly in G2, while their number remains similar.

### PB purification reveals the same major PB proteins across the cell cycle

To characterize changes in PB composition during cell cycle progression, we set out to purify them from different phases of the cell cycle using our previously developed Fluorescence Activated Particle Sorting (FAPS) method[7] (Figure 1C) and HEK293 cells that stably express GFP-LSM14A at levels similar to endogenous LSM14A (Figure S2A). In these cells, GFP-LSM14A co-localizes with the PB marker DDX6 (Figure S2B) but not the stress granule marker TIA1 (Figure S2C). We selected 4 cell cycle stages for their biological significance: mid G1, G1S transition, mid S and G2M transition. Cells were synchronized using two complementary

131 strategies (Figure 1D): (i) a double thymidine block to harvest cells blocked at the G1S transition,
132 after which they were released for 5 hr to obtain cells in mid S phase; (ii) a selective CDK1
133 inhibitor[29] (RO-3306) to block cells at the G2M transition, after which they were released for 8 hr
134 to obtain cells in mid G1. Forty 15 cm plates were synchronized per phase to obtain sufficient
135 material for FAPS purification. The quality of the synchronization was assessed on a small fraction
136 of each plate by propidium iodide staining of the DNA followed by flow cytometry analysis (Figure
137 1D). After synchronization, cytoplasmic lysates were prepared as described in the Materials and
138 methods. An aliquot was kept aside for further analysis and thereafter termed the pre-sorting
139 fraction (PSF). Two controls were used to delineate the PB sorting window (Figures 1E): (i) cell-
140 free lysis buffer and (ii) a lysate from cells expressing a truncated GFP-LSM14A protein that only
141 displays diffuse GFP fluorescence (Figure S2D). For all cell cycle phases, PBs were sorted based
142 on particle size and GFP fluorescence (Figures 1E and S3). After sorting, a fraction of the purified
143 sample was re-analyzed by flow cytometry (Figures 1E and S3) and visualized in fluorescence
144 microscopy (Figure 1F) to verify that PBs were conserved while cytoplasmic contaminants were
145 considerably reduced.

146 After a total of >140 hr sorting, sufficient material was accumulated for proteomic analysis
147 of PBs from each cell cycle phase, using liquid chromatography-tandem mass spectrometry (LC-
148 MS/MS, Supplementary Table 1). In all phases, the vast majority of known PB proteins (17-29
149 proteins detected) were enriched in the purified PB fraction compared to the PSF (Figures 1G
150 and S4). These included translational repressors and RNA decay factors (including DDX6,
151 LSM14A and LSM14B, 4E-T, EDC4 and DCP1A) and proteins of the miRNA pathway (AGO1-3
152 and MOV10). In contrast, proteins such as mitochondrial proteins, translation initiation factors,
153 components of the proteasome, splicing factors and histones were mostly depleted (Figures 1G
154 and S4A). We then asked if the protein content of PBs changed during cell cycle. Given the
155 inherently limited amounts of proteins obtained from purified PBs, we could not carry out the
156 replicates needed for quantitative MS. Nevertheless, a pairwise comparison of PBs from
157 successive cell cycle phases did not show drastic changes in the levels of the well-detected PB
158 proteins (Figure 1H). In summary, the proteomic analysis of purified PBs does not show major
159 changes of the main PB proteins across the cell cycle.

160

161 **PB RNA content is dynamic during cell cycle progression**

162 We then analyzed the RNA content of the purified PBs and their corresponding PSFs using RNA
163 sequencing. First, to assess if the PSFs recapitulated known cell cycle-dependent RNA
164 regulation, we took advantage of a published study that compared G1S to G2M HeLa cells[30]. Most
165 RNAs reported as more expressed in G1S or in G2M were indeed more abundant in our G1S or
166 G2M PSFs, respectively, despite the different cell line and protocols (Figure S5A). Then, gene
167 ontology (GO) analysis showed that RNAs more abundant in our G2M sample encode proteins
168 involved in chromatin condensation, chromosome segregation, and cell division, while those more
169 abundant in G1S encode proteins involved in nucleotide metabolism, DNA replication and its
170 regulation (Figure S5B,C). Altogether, these analyses confirmed the reliability of our
171 transcriptomic data for cell cycle analysis. We then compared RNA levels before and after sorting
172 within each cell cycle phase (Figures 2A and S6). Between 3,838 and 5,106 mRNAs were
173 enriched in PBs (p-adj<0.05, DEseq2 model[31]) depending on the cell cycle phase (Supplementary
174 Table 2). Among them, 2043 were enriched in only a subset of phases or at a unique phase
175 (Figure 2B).

176 Next, we compared the RNA content of purified PBs across the cell cycle (Supplementary
177 Tables 3 and 4, Figure S7). Remarkably, this revealed widespread changes in RNA levels in PBs
178 (Figures 2C and S8A). For example, from mid G1 to G1S, 2943 mRNAs had increased levels in
179 PBs, while 2599 decreased (Figure 2C, D). To determine if the mRNAs with cyclic accumulation
180 in PBs encode proteins enriched for specific functions, we systematically performed GO analyses.
181 We found that mRNAs accumulating in PBs between mid G1 and mid S were enriched (181 out
182 of 1889) for transcripts encoding proteins functioning in mitotic cell cycle phase transition,
183 chromosome condensation, and cytokinesis (Figure 2E, left panel). Inversely, the mRNAs that
184 decreased in PBs between mid G1 and mid S were enriched (154 out of 1813) for transcripts
185 encoding proteins involved in transcription, transcriptional regulation, and RNA-binding (Figure
186 2E, right panel). Taken together, this indicated that the mRNA content of PBs is highly dynamic
187 throughout the cell cycle.

188

189 **RNA accumulation in PBs is in part uncoupled from their cytoplasmic expression level**

190 Cell cycle variations in mRNA levels have been well characterized and are controlled at the levels
191 of transcription and/or stability[13,17–20,22,23,30]. The question here was whether there is specific
192 regulation at the level of mRNA localization in PBs. In a scenario where there is none, we expect
193 mRNA levels in PBs to closely follow their level in the cytoplasm across phases. We therefore

194 investigated the relationship between the RNA content of PBs and the surrounding cytoplasm,
195 using PSFs as a proxy for cytoplasms. Comparing the RNA changes in PBs and PSFs from mid
196 G1 to G1S indeed showed an overall distribution along the diagonal (Figure 2F), suggesting a
197 broad coupling between the RNA content of PB and cytoplasm. Yet, when mRNAs decreased in
198 PBs between the two phases, their decrease was twice less pronounced in the cytoplasm.
199 Moreover, many cases fell far from the general distribution, as exemplified by FBXO5 and CLK1
200 mRNAs (studied later), indicating some degree of uncoupling between the PB and cytoplasm
201 contents. The results were similar from G1S to mid S. In contrast, from mid S to G2M the PB
202 content was weakly coupled to the prominent transcriptional induction. For example, the PB
203 fraction did not mirror the cytoplasmic increase in TOP2A, BUB1B, and CENPF levels (Figure 2F,
204 studied later). Similarly between G2M and mid G1, the PB content did not follow the prominent
205 decrease of cytoplasmic transcripts. In conclusion, these data suggest that the dynamics of the
206 PB transcriptome can be uncoupled from cytoplasmic variations, particularly during the 2$^{nd}$ half of
207 the cell cycle, setting the stage for cell cycle-dependent RNA targeting to PBs.

208

209 **In-situ confirmation of various patterns of cyclic RNA localization in PBs**

210 Our transcriptomic analysis revealed cell cycle-dependent changes in the RNA content of PBs.
211 To supplement these genome-wide analyses, we performed single molecule FISH (smFISH)
212 experiments on several mRNAs (candidates chosen based on PB-enrichment pattern, p-adj
213 values, and sufficient expression levels for reliable smFISH detection). smFISH illuminates
214 individual RNA molecules *in-situ*, allowing localization and counting of RNA molecules[32,33].

215 We started with the mRNA of the cell cycle protein FBXO5, a major regulator of the
216 anaphase promoting complex (APC)[34–39]. In our RNA-seq dataset, FBXO5 expression was
217 highest in G1S and mid S phases in the PSF, in accordance with its transcriptional induction at
218 G1S[40]. In purified PBs, it also peaked at G1S and mid S, but with a much higher differential with
219 mid G1 or G2 (Figure 3A). For smFISH, we synchronized HEK293 cells expressing GFP-LSM14A
220 in G1S, mid S, G2M and mid G1, as performed for PB purification. In agreement with the RNA-
221 seq data, we observed more FBXO5 mRNA molecules in the cytoplasm, and considerably more
222 in PBs, in G1S and mid S than in G2M and mid G1 (Figure 3B). This was confirmed by quantitative
223 image analysis (Figure 3C), which showed that the fraction of FBXO5 mRNAs localized in PBs
224 cycled between ~25% in mid G1 and ~63% in mid S (Figure 3C).

225 Similarly, we examined the mRNAs encoding the cell cycle-regulated splicing factor
226 CLK1[41] and cyclin E2 (CCNE2). In contrast to FBXO5, CLK1 transcripts gradually increased in
227 both PBs and the cytoplasm throughout the cell cycle, peaking at G2M (sequencing data and
228 smFISH experiments, Figures 3A,D). Quantitation of the smFISH images indicated that the
229 fraction of RNA in PBs increased from ~38% of the molecules in mid G1 and G1S to ~48% in
230 G2M (Figure 3E). CCNE2 transcripts had a similar profile as FBXO5, with both sequencing data
231 and smFISH experiments showing maximal cytoplasmic and PB levels in G1S (Figure 3A,F), with
232 the fraction of CCNE2 mRNA molecules in PBs oscillating between ~31% in G1S and ~25% in
233 G2M (Figure 3G). Thus, CCNE2, FBXO5 and CLK1 mRNAs exhibited various PB localization
234 patterns, peaking at G1S, mid S, and G2M, respectively. To summarize, these smFISH
235 experiments provided single-molecule evidence of cyclic mRNA accumulation in PBs across the
236 cell cycle.

237

238 **PBs capture a subset of cyclic mRNAs after mitotic exit**

239 We next focused on mRNAs harboring prominent induction in the cytoplasm in G2 though with
240 limited consequences on PB accumulation (Figure 2F). We first analyzed the mRNA encoding
241 the G2 protein topoisomerase 2A (TOP2A), which regulates chromosome compaction[42] and
242 relieves topological DNA stress[43,44]. In the sequencing dataset, expression of TOP2A increased
243 slightly from mid G1 to S and significantly more in G2M, as previously described[45–47]. This
244 increase however was not mirrored in PBs where TOP2A mRNA levels remain similar from mid
245 G1 to G2M (Figure 4A). SmFISH experiments on asynchronous cells revealed three TOP2A
246 localization patterns: (i) some cells had few TOP2A mRNA molecules in both the cytoplasm and
247 PBs (Figure 4B, white arrows); (ii) others showed high TOP2A mRNA expression in the cytoplasm
248 but modest localization in PBs (Figure 5B, yellow arrows); and, to our surprise, (iii) a subset of
249 cells showed heavy TOP2A mRNA accumulation in PBs with few TOP2A mRNA molecules free
250 in the cytoplasm (Figure 4B, green arrows). Quantitative image analysis further assessed this
251 striking heterogeneity (Figure 4C). TOP2A biology[48] and our RNA-seq data suggested that cells
252 with high RNA expression and low PB localization (pattern ii) corresponded to G2 cells, i.e. when
253 the protein is needed and most highly expressed. We speculated that after mitosis, in early G1 (a
254 time point not included in the PB purification pipeline, but accessible with smFISH), leftover
255 TOP2A mRNA could be sent to PBs (pattern iii). To test this hypothesis, we transiently expressed
256 Halo-tagged LSM14A in HEK293-FUCCI cells to allow for the simultaneous imaging of
257 cytoplasmic TOP2A mRNAs, PBs and nuclear PIP-FUCCI cell cycle markers. As expected, S and

258 G2 cells showed high levels of TOP2A mRNA with modest PB localization (Figure 4D, red and
259 yellow arrows). In contrast, G1 cells showed two patterns, with either minute amount of TOP2A
260 mRNAs, or moderate TOP2A expression but striking accumulation in PBs (Figure 4D, green
261 arrows). Since TOP2A remains abundant during mitosis[47] (Figure 4D, white arrow) and is
262 transcriptionally induced only in G1S or early S[49,50], we conclude that the latter cells correspond
263 to early G1 where residual TOP2A mRNAs are localized in PBs. To summarize, the burst of
264 TOP2A mRNA expression in G2 cells, when the protein is needed, does not coincide with PB
265 accumulation. Rather, localization in PBs occurs when they reform in early G1, at a time when
266 TOP2A mRNA is down regulated and the protein no longer required.

267 Looking for mRNAs with similar expression patterns as TOP2A in our transcriptomic
268 dataset, we identified mRNAs encoding the centromere protein F (CENPF) and, to a lesser extent,
269 the mitotic checkpoint serine/threonine kinase B (BUB1B) (Figure 4A). Like TOP2A, these mRNAs
270 are most highly expressed in G2 and encode proteins functioning mainly in G2 and mitosis:
271 CENPF is essential for kinetochore function[51,52] while BUB1B ensures proper attachment of
272 chromosomes to the mitotic spindle[53,54]. Using 2-color smFISH, we found that CENPF and BUB1B
273 mRNAs had indeed similar dynamics as TOP2A: they co-localized with it in PBs in early G1 cells
274 (Figure 4E, blue arrows), and were highly expressed yet weakly present in PBs in S or G2 cells
275 (Figure 4E, yellow arrows). As a benchmark, we took advantage of PUM2 mRNA, which displayed
276 a similar expression and PB localization throughout the cell cycle in our transcriptomic dataset
277 (Figure 4A) and in the 2-color smFISH (Figure 4E). In summary, a group of transcripts encoding
278 G2-M proteins traffic into PBs after cell division, when their protein is no longer needed. Such an
279 observation further highlights that RNA accumulation in PBs can vary independently of its
280 cytoplasmic abundance and thus contribute to mRNA regulation.

281

282 **A subset of mRNAs decaying at the mitosis-to-G1 transition specifically accumulate in PBs**
283 **in G1**

284 In a parallel approach to FAPS, we set out to explore RNA localization in PBs across the cell cycle
285 using high-throughput smFISH (HT-smFISH, Figures 5A, S9). We selected 94 mRNAs with or
286 without known cyclic expression and carried out the analysis in non-synchronized HEK293 cells
287 expressing GFP-LSM14A. Cells were classified in G1 or G2 phase based on their DAPI signal.
288 Briefly, for each imaged RNA, the integrated DAPI signal was used to construct a cell cycle profile,
289 which allowed to separate cells in G1 or G2 phase with high confidence (example profile in Figure

290 5A, see Methods for details). While most transcripts displayed a similar fraction in PBs in G1 and
291 G2 cells, a subgroup of mRNAs showed higher mRNA accumulation in PBs in G1 than in G2
292 (Figure 5B). Single-cell representation of such transcripts showed that the fraction of mRNA in
293 PBs was particularly heterogeneous in G1 cells, readily reaching values above 50% of mRNA
294 molecules (Figure 5C). Interestingly, expression of many of these transcripts was reported to peak
295 in G2 and decrease in G1, while their encoded proteins are implicated in G2-to-mitosis
296 progression (such as ECT2[55], TTK[56], and DLGAP5[57]).

297 We therefore hypothesized that mRNA accumulation in PBs may be concomitant with their
298 elimination after mitosis. Among the 94 mRNAs included in our HT-smFISH, 17 were previously
299 reported to undergo decay at the mitosis-to-G1 (M-G1) transition[22]. Remarkably, most mRNAs
300 showing higher accumulation in PBs in G1 than in G2 cells belonged to this group (Figure 5B-D
301 and G, upper panels). Conversely, mRNAs encoding G2 proteins but not undergoing decay at the
302 M-G1 transition accumulated similarly in PBs in G2 and G1 cells (Figure 5B-D and G, lower
303 panels). To extend these data, we considered the 161 mRNAs described as decaying at the M-
304 G1 transition[22] and well detected in our FAPS dataset. 62% of them were significantly enriched in
305 PBs purified from G1 cells, which is higher than expected (44% for all mRNAs, Figure 5E). They
306 also tended to be enriched in PBs to greater extents (Figure 5F). Taken together, HT-smFISH
307 independently provides evidence of cell cycle-dependent RNA localization in PBs, with a subset
308 of mRNAs undergoing M-G1 transition decay specifically accumulating in PBs in G1 phase.

309

310 **Cyclic mRNA localization in PBs does not result from fluctuating amounts of non-**
311 **polysomal mRNAs**

312 To better understand cyclic mRNA localization in PBs, we first envisioned a mechanism related
313 to the condensate nature of PBs. The examples studied above clearly showed that mRNA
314 localization in PBs does not follow expression changes in the cytoplasm throughout the cell cycle.
315 Nevertheless, PBs could be more subtly involved in attenuating cell-to-cell expression differences
316 within the same cell cycle stage, a mechanism suggested from an artificial condensate study[58].
317 To address this hypothesis, we used the quantitative analysis of the cell cycle-resolved TOP2A,
318 FBXO5, and CLK1 smFISH experiments described above. Even within the same cell cycle phase,
319 the fraction of mRNAs in PBs showed weak or no correlation with cytoplasmic expression (Figure
320 S10A). This was true whether RNA fractions in PBs were high or low (e.g. TOP2A mRNAs in early

321 G1 vs S or G2, respectively), and argued against a general role of PBs in recruiting excess
322 cytoplasmic mRNAs.

323 Alternatively, PBs could simply recruit mRNAs when they are free in the cytoplasm. In this
324 scenario, the distinctive TOP2A, BUB1B, and CENPF mRNA localization pattern could result from
325 their specific translational downregulation after mitosis, driving free mRNAs into newly formed
326 PBs. In that case, disrupting polysomes should be sufficient for their untimely recruitment in PBs
327 in G2. To test this, we treated HEK293-FUCCI cells transiently expressing LSM14A-Halo with
328 puromycin. This translation inhibitor disrupts polysomes within a few minutes, disassembling
329 ribosomes and the translation machinery from the mRNA and releasing nascent peptides[59].
330 Interestingly, a 1 hr puromycin treatment did not cause TOP2A mRNAs to massively relocalize
331 into PBs in G2 cells (Figure S10B). Similarly, 2-color smFISH of BUB1B or CENPF mRNAs with
332 TOP2A mRNAs in the HEK293 cell line expressing GFP-LSM14A did not show significant
333 difference of localization in PBs between control and puromycin-treated cells (Figure 6A-D). The
334 efficiency of the puromycin treatment was controlled using HeLa cells expressing endogenous
335 ASPM-MS2 mRNA that localizes to centrosomes in a translation-dependent manner[60,61]. As
336 expected, centrosomal localization of this mRNA was abolished after a 15 min puromycin
337 treatment (Figure S10C). In summary, disrupting polysomes was not sufficient to prematurely
338 drive TOP2A, BUB1B, and CENPF mRNAs into PBs in G2 phase.

339

340 **Long CDSs favor accumulation of AU-rich mRNAs in PBs in early G1**

341 We then searched for mRNA features that could participate in cell cycle-dependent PB
342 localization. We previously reported that in asynchronous cells, the GC content of CDS and 3'UTR
343 is the best predictor of mRNA enrichment in PBs[8]. This held true at all cell cycle phases: PB-
344 enriched mRNAs were particularly AU-rich, with a striking correlation between PB enrichment and
345 GC content ($r_s$ between -0.75 and -0.79 for the GC content of the mRNA, Figure S11A, B).
346 However, this compositional bias displayed only minor changes across the cell cycle. Even
347 focusing on the top 1000 PB-enriched mRNAs did not reveal any notable difference between cell
348 cycle phases (Figure S11C). Given the nucleotide bias in the CDS, NNA/U triplets were strongly
349 overrepresented in PB-enriched mRNAs, as observed previously[8] (Figure S11D). While this
350 codon usage bias is similar to one reported for cell cycle-regulated genes[62] (Figure S11E), it
351 appeared unrelated to cell cycle-regulated PB localization (Figure S11D).

352 We also reported that PB-enriched mRNAs tend to be longer than average[8]. While this
353 held true at all cell cycle phases (Figure S11F), the correlation between PB enrichment and mRNA
354 length was higher in G1 phase than in the other phases ($r_s$ of 0.33, compared to 0.20-0.24, Figure
355 S11G). The analysis of the top 1000 PB-enriched mRNAs further revealed striking differences
356 between cell cycle phases. These mRNAs were much longer than average in mid G1 (5.1 kb
357 median, compared to 3.3 kb), shorter in G1S and S (4.2 and 4.4 kb, respectively), and similar to
358 average in G2 (3.5 kb, Figure 7A). The size differences mainly originated from the CDS, since
359 3'UTR exhibited less striking differences (Figure 7A). Similarly, mRNAs revealed by HT-smFISH
360 to accumulate more in PBs in G1 than in G2, had particularly long CDS (Figure S11H).
361 Furthermore, for the top 500 AU-rich mRNAs, CDS length appeared as a key feature associated
362 with PB localization in G1 ($r_s$=0.63) but not in G2 ($r_s$=-0.07, Figure S11I). These results suggested
363 that the CDS length plays an important role in the accumulation of the most AU-rich mRNAs in
364 PBs in G1 but not in G2 phase.

365 To investigate if a long CDS directly contributes to driving mRNAs into PBs in G1, we
366 transiently transfected two Renilla Luciferase reporters, with either a 0.9 kb or a 1.7 kb CDS
367 (obtained by lengthening Renilla while keeping a similar GC content) in HEK293 cells expressing
368 GFP-LSM14A. Importantly, both CDSs were AU-rich (36% GC), making them amenable to PB
369 localization[8]. We then performed a 2-color smFISH against Renilla and TOP2A mRNAs to
370 distinguish early G1 from S and G2 cells (Figure 7B, C). In early G1 cells, the long CDS reporter
371 accumulated significantly more in PBs than the short one, while in S and G2 cells both reporters
372 minimally accumulated in PBs (Figure 7D). This indicated that a longer CDS increases RNA
373 accumulation in PBs specifically in early G1. Taken together, these data show that CDS length,
374 in the context of an AU-rich nucleotide composition, is a feature that contributes to RNA
375 accumulation in PBs specifically in G1 cells.

376

377 **Discussion**

378

379 **The mRNA content of PBs is dynamic and partly uncoupled from the cytoplasmic content**

380 In this study, we set out to investigate the dynamics of mRNA localization in PBs at the scale of
381 hours in standard growth conditions. As a biological context, we chose the cell cycle since it entails
382 changes in cytoplasmic RNA abundance that have been well documented at various RNA
383 metabolism levels[13–15,18,19,21,22,22]. During every cell cycle, PBs form in G1, then increase in size
384 more than in number, culminating in G2, before dissolving in mitosis. Cycling cells thus give
385 access to the cell-autonomous dynamics of PB RNA content in the absence of any stress.

386 PB purification from various stages of the cell cycle provided us with a genome-wide
387 landscape of PB RNAs during cell cycle progression. This allowed us to answer the primary
388 question: does the RNA content of PBs change during cell cycle progression? We observed
389 indeed that, despite no major changes in their main protein composition, PBs undergo widespread
390 changes in their mRNA content. Secondly, do these changes simply mirror changes of
391 cytoplasmic mRNA abundance, or do they behave distinctly? In fact, part of these changes did
392 not reflect those of the cytoplasm: (i) mRNAs could change in PBs more strikingly than in the
393 cytoplasm (particularly from mid G1 till mid S), (ii) and inversely, they could markedly change in
394 the cytoplasm without a similar change in PBs (particularly from mid S to the next G1). Single
395 molecule RNA imaging confirmed the reliability of our PB transcriptomes across the cell cycle and
396 highlighted the remarkable variety in RNA localization patterns: for example, TOP2A, BUB1B and
397 CENPF strikingly accumulated in PBs in early G1; many mRNAs peaking in G2 before undergoing
398 decay accumulated in PBs in G1; CCNE2 at the G1S transition; FBXO5 in mid S; and CLK1 at
399 the G2M transition. Thus, differential localization in PBs is not restricted to specific stages of the
400 cell cycle. In particular, it does not follow the evolution of PBs considered as a whole (increasing
401 size and number) during cell cycle progression. This positions RNA localization in PBs as a
402 potential gene-specific post-transcriptional regulatory layer operating across the cell cycle.

403

404 **Biological relevance of differential mRNA accumulation in PBs**

405 Can differential RNA accumulation in PBs contribute to cell biology? One possibility involves
406 sequestering mRNAs when the protein is not needed anymore. This is illustrated by TOP2A,
407 CENPF and BUB1B mRNAs, which strongly accumulated in PBs in early G1. These transcripts
408 are transcriptionally and translationally upregulated from late S to mitosis, periods when their

409 encoded protein is needed[48,49,49,52,54], and then subject to mitotic decay pathways[22]. TOP2A
410 mRNA for instance is degraded by a CCR4-NOT-dependent mechanism[22]. However, when the
411 process is not fast enough to completely prevent protein production in G1, there is no mechanism
412 for ensuring translation inhibition of its residual transcripts in G1[22,63]. We hypothesize that PB
413 localization could contribute to the silencing of such transcripts in early G1. These few examples
414 are further corroborated by our HT-smFISH analysis which revealed a group of mRNAs that
415 specifically accumulated in PBs in G1, that are also subject to mitotic decay[22]. Regardless of how
416 and where their decay is taking place, our data suggest that PBs offer a safety net to attenuate
417 mistimed protein production of cell cycle regulators by compartmentalizing their mRNAs away
418 from the translation machinery.

419 **PBs do not buffer excess non-polysomal mRNAs**

420 What can be the mechanism underlying cyclic mRNA localization in PBs? We first envisioned a
421 mechanism inspired by the physical nature of membraneless organelles. Since liquid-liquid phase
422 separation (LLPS) implies the condensation of molecules that are over their saturation
423 concentration, membraneless organelles have been proposed as a buffering mechanism to limit
424 cell-to-cell variability of intracellular concentration[58]. In this context, mRNA accumulation in PBs
425 may increase for some transcripts in a particular cell cycle phase due to higher heterogeneity of
426 expression. Our single molecule FISH data did not support such a hypothesis. For all mRNAs
427 analyzed, despite wide cell-to-cell variability of expression within a given cell cycle phase, we
428 observed no or limited correlation between mRNA accumulation in PBs and in the cytoplasm. This
429 is consistent with the observation that, in contrast to minimal condensates like the recently
430 described nanoclusters forming upon massive mRNA storage in C. elegans arrested oocytes[64],
431 multicomponent cellular organelles like nucleoli or stress granules, are not governed by a fixed
432 saturation concentration[65].

433 Then, since polysomal mRNAs are excluded from PBs, we considered a scenario where
434 mRNA accumulation in PBs would be governed by the amount of non-translating mRNAs. From
435 a transcriptome-wide perspective, it has been previously proposed that non-optimal codon usage
436 could generate cell cycle-dependent translation efficiency[62]. In all cell cycle phases, we found that
437 PB-enriched mRNAs were particularly AU-rich, leading to a non-optimal codon usage associated
438 with inefficient translation, as described previously[8]. However, neither the GC content, nor the
439 codon usage of PB-enriched mRNAs differed between phases, indicating that codon usage is not
440 involved in the cyclic pattern of mRNA accumulation in PBs. We also addressed the question
441 experimentally on endogenous mRNAs that have the capacity to accumulate in PBs (TOP2A,

442 BUB1B and CENPF). Releasing these mRNAs from polysomes in G2 cells was not sufficient to
443 relocate them in PBs, despite them having appropriate intrinsic features to accumulate in PBs in
444 early G1. Altogether, we did not find evidence that mRNA accumulation in PBs represents only
445 the inverted mirror of mRNA translation.

446

447 **CDS length contributes to RNA localization in PBs in G1 but not G2**

448 This prompted us to look for other intrinsic determinants of cell cycle-dependent mRNA
449 localization in PBs. We previously reported that mRNA accumulation in PBs in asynchronous cells
450 moderately correlated with their length[8]. To our surprise, this feature was cell cycle-dependent,
451 with PB mRNAs one and a half times longer in G1 than in G2 (5.1 vs 3.5 kb), the latter being close
452 to average. Their 3'UTR tended to be longer than average in all phases, consistent with the
453 hypothesis that they bring binding motifs for translation repressors that favor recruitment in PBs,
454 as discussed previously[8]. In contrast, the CDSs of PB-enriched mRNAs were particularly long in
455 mid G1 but not G2M, reaching one a half time the average length (2.3 vs 1.5 kb). Moreover, for
456 the most AU-rich mRNAs of the transcriptome, CDS length correlated with PB enrichment in G1
457 but not G2M. Critically, we confirmed using an mRNA reporter that CDS length had more impact
458 in early G1 than in S or G2. Since translational blockage did not alter cyclic RNA accumulation in
459 PBs, it is unlikely that differential localization across the cell cycle is linked to the coding capacity
460 of the CDS. Instead, we speculate that some RBPs that preferentially bind long CDSs and play a
461 role in mRNA recruitment into PBs are expressed or post-translationally modified at precise cell
462 cycle stages.

463 From a LLPS perspective, we favor an alternative non-exclusive possibility. Modeling and
464 simulations have shown that longer transcripts localize at the core of RNA-protein condensates,
465 where they augment the density of molecular interactions and saturate chemical bonds[66,67]. This
466 promotes LLPS and stabilizes condensates, preventing collapse from excessive RNA
467 recruitment. These in-silico observations seem to fit well the cell cycle dynamics of PBs, which
468 form in G1, progressively grow through the cell cycle and dissolve in mitosis. It is particularly
469 tempting to speculate that long RNAs favor the seeding and stabilize nascent PBs in early G1.
470 These PBs could then progressively accumulate more RNA, growing into "mature" PBs without
471 collapsing. Long RNAs may at a certain point lose their advantage, because the interaction
472 network is sufficiently stable and saturated, or also because short RNAs, which are modeled to
473 localize at the surface of condensates[66], may provide a barrier to long RNA recruitment[68].Such a

474 model would be also particularly relevant for stress-induced membraneless organelles like stress
475 granules, which were shown to contain particularly long mRNAs after a 1 hr induction[69].

476 Taken together, mRNA accumulation in PBs appears to be a multifaceted process
477 involving the cumulative effect of intrinsic (GC content, CDS length) and extrinsic (RBPs) factors.
478 If PBs are highly dynamic condensates in a cell-autonomous process like cell cycle progression,
479 they should be even more so across a whole organism, during development and differentiation,
480 and in a changing environment or in response to stress.

481 **Methods**

482

483 **Cell culture, drug treatments, and transfections**

484 HEK293 and HeLa cells were grown in Dulbecco's modified Eagle's Medium (DMEM, Gibco)
485 supplemented with 10% fetal bovine serum (FBS, Sigma-Aldrich), and 100 U/mL
486 penicillin/streptomycin (Sigma-Aldrich). HEK293 cells stably expressing GFP-LSM14A were
487 obtained by transfecting a pCMV-GFP-LSM1A plasmid and selecting stable clone under 500
488 µg/mL G418 (Gibco). HEK293-FUCCI cells were obtained via CRISPR-Cas9-mediated insertion
489 of the PIP-FUCCI reporter in the AAVS1 genomic locus and selection under 1 µg/mL puromycin.
490 All cells were grown at 37 °C with 5% $CO_2$. To inhibit translation, cells were treated with 100
491 µg/mL puromycin for 1 hr or 15 min, as indicated. For all transient transfections, 5 µl Lipofectamine
492 2000 (Thermo Fisher Scientific) was used with the following DNA quantities per well of a 6-well
493 plate: 1 µg LSM14A-Halo tag, and 100 ng of each Renilla luciferase construct with 900 ng of a
494 non-transcribed plasmid. All transfection were done for 5 hr after which the reagent was washed
495 off and cells allowed to grow for 24-48 hr before fixation. Cell fixation was done with 4%
496 paraformaldehyde PFA (Electron Microscopy Sciences) for 20 min at room temperature (25°C).
497 The Renilla Luciferase short (0.9 kb) and long plasmids (1.7 kb) were expressed under a CMV
498 promoter.

499

500 **Synchronizations**

501 All synchronizations were performed in HEK293 cells expressing GFP-LSM14A. For PB
502 purification, synchronizations were done in 15 cm dishes. For double thymidine blocks, 4 million
503 cells were seeded. The next day, 7.5 mM thymidine was added to the culture medium for 18 hr.
504 Cells were then washed gently with warm PBS three times and further incubated in fresh complete
505 medium. Cells were released for 9 hr after which 7.5 mM thymidine was added again for another
506 18 hr. This results in cells blocked at the G1S transition. To obtain cells in mid S phase, cells were
507 further washed three times in warm PBS after which fresh complete medium was added. Cells
508 were released for 5 hr to obtain a population at mid S phase. For CDK1 inhibition, 8 million cells
509 were seeded. The next day the CDK1 inhibitor RO-3306 was added at 9 µM. After 22 hr, cells
510 blocked at the G2M transition were harvested. To obtain cells at mid G1, we found that half the
511 drug's concentration (with the same blockage time) provides a better release from G2M into mid
512 G1 (with three PBS washes and an 8 hr release in fresh complete medium). Forty to fifty 15 cm

513 dishes for each cell cycle phase were synchronized. After each synchronization, a small fraction
514 of each 15 cm dish was tested in flow cytometry for the quality of the synchronization and, if
515 synchronization reached 55% for mid G1, 80% for G1S or mid S, and 70% for G2M, the rest was
516 used for PB purification. For microscopy experiments, identical synchronizations were done for
517 cells grown on 22x22 cm coverslips in 6-well plates, with the addition of poly-L-lysine for better
518 cell adhesion.

519

520 **Cell cycle related flow cytometry analysis and FACS purification**

521 To fix cells for flow cytometry analysis, ~100,000 cells were washed twice in PBS, trypsinized,
522 and suspended in PBS. Cells were pelleted at 500 g for 5 min at 4°C and the pellet resuspended
523 in 300 µl ice-cold PBS to which 900 µl cold ethanol (100% vol/vol) was slowly added. Cells were
524 stored at -20°C overnight to allow fixation. The next day, cells were pelleted at 500 g for 5 min at
525 4°C. To label DNA, cells were resuspended in a 500 µl solution of 20 µg/mL RNaseA and 50
526 µg/mL propidium iodide in PBS and incubated at 37°C for 30 min. Flow cytometry was performed
527 on a MACSQuant® Analyzer 10 Flow Cytometer (Miltenyi Biotec) using the 561 nm laser and
528 acquisitions analyzed using FlowJo (v10.6.2). For flow cytometry analysis of living HEK293-
529 FUCCI cells: cells grown to 80% confluency in 6-well plates were washed three times in PBS,
530 trypsinized, and suspended in PBS. Cells were then pelleted for 5 min at 500 g at room
531 temperature (25°C). The pellet was then resuspended in complete DMEM medium containing 15
532 µg/mL Hoechst 33342 (Life technologies, H3570) and incubated for 30 min at 37°C before flow
533 cytometry analysis. Cytometry and analysis were performed using the same hardware (with a 405
534 nm laser) and software.

535 To sort HEK293-FUCCI cells by FACS: cell were grown to 80% confluency in 10 cm dishes
536 and processed identically, minus the Hoechst 33342 staining. Around 1.5-2 million cells were
537 sorted for each cell cycle phase (G1, S, or G2/M) using a MoFlo Astrios EQ (Beckman-Coulter,
538 488 and 561 nm lasers) and collected cells were pelleted for 5 min at 500 g. Cell pellets were
539 flash frozen every 30 min to minimize the amount of cells transitioning into the next cell cycle
540 phase and accumulated for western blotting.

541

542 **PB purification by FAPS**

543 PB purification by FAPS was performed as described previously[7], with a few modifications.
544 HEK293 cells stably expressing GFP-LSM14A (synchronized or not) were allowed to grow to ~70-
545 80% confluency in 15 cm dishes. After two PBS washes, cells were scrapped off, collected in 2
546 ml Eppendorf tubes and pelleted at 500 g for 5 min. Pellets were flash frozen in liquid nitrogen
547 and stored at -80°C until the day before sorting. Each cell pellet was then resuspended in 1.5 mL
548 ice-cold lysis buffer containing 50 mM Tris pH 8, 1 mM EDTA, 150 mM NaCl, and 0.2% Triton X-
549 100 supplemented with 65 U/mL RNase out (Promega) and 2x protease inhibitor cocktail (Roche),
550 pipetted a few times and kept on ice for 20 min. Then, nuclei were pelleted by centrifugation for 5
551 min at 500 g, and the supernatant containing cytoplasmic organelles, including PBs, was
552 transferred to a new tube. After supplementation with 10 mM $MgSO_4$, 1 mM $CaCl_2$, and 4 U/mL
553 RQ1 DNase (Promega), samples were incubated at room temperature (25°C) for 30 min while
554 avoiding direct sources of light to avoid GFP fluorescence bleaching. Next, the samples were
555 centrifuged at 10,000 g for 7 min at 4°C. The supernatant was gently aspirated and the pellet was
556 resuspended in 30 µl lysis buffer supplemented with 40 U RNase out. This was called the pre-
557 sorting fraction. A small aliquot (1-3 µL) was stained with ethidium bromide and visualized using
558 widefield fluorescence microscopy for a reference image before sorting. For each cell cycle
559 phase, 3 independent pre-sorting fractions were kept aside for RNA-seq and mass spectrometry
560 analyses to compare with their sorted counterparts.

561 Fluorescence activated particle sorting (FAPS) was carried out on a MoFlo Astrios EQ
562 (Beckman-Coulter) using the 488 nm excitation laser. The PB sorting gate was determined using
563 control samples of lysis buffer alone, or an identical cell preparation but made with cells
564 expressing truncated GFP-LSM14A that does not localize in PBs (GFP-LSM14A-Δ, described in
565 [7]). The pre-sorting sample was diluted 30 times in lysis buffer at the time of sorting (10 µL in 300
566 µL lysis buffer). The differential pressure during sorting was maintained around 0.8 and the sorting
567 speed was around 8,000 events per second on average. The sorting purity was >95%. After
568 sorting, a small aliquot was stained with ethidium bromide, and visualized under widefield
569 fluorescence microscopy. Purified PBs were pelleted at 10,000 g for 7 min in 2 mL Eppendorf
570 tubes, while the remaining was stored at -80°C. ~6 hr of active sorting were done per day and 2-
571 3 days of sorting output were combined together to constitute a single replicate for RNA-seq for
572 each cell cycle phase. A total of >140 hr of FAPS was needed to accumulate sufficient material
573 for RNA-seq in triplicates and 1 mass spectrometry analysis for each of the 4 cell cycle conditions.
574 Protein and RNA were extracted using TRIzol (Thermo Fisher Scientific). A total of ~400 ng
575 protein per condition and 5-10 ng RNA per replicate per condition were obtained.

576

577 **Mass spectrometry**

578 Liquid chromatography–tandem mass spectrometry (LC-MS/MS) was performed at the
579 proteomics platform at Institut Jacques Monod, Paris France. Proteins from the purified PB or pre-
580 sorting fractions were dissolved in a 8 M urea solution (Sigma-Aldrich) before trypsin digestion.
581 Samples were analyzed using an Orbitrap Fusion Lumos Tribrid Mass Spectrometer (Thermo
582 Fisher Scientific) with the following settings: Ion Source: ESI (nano-spray), Fragmentation Mode:
583 high energy CID, MS Scan Mode: FT-ICR/Orbitrap. Peptide and protein signals were processed
584 using PEAKS Studio (v10.6 build 20201015) with the following parameters: Max Missed
585 Cleavages: 2, Database: Homo Sapiens SwissProt Release_2020_06, Parent Mass Error
586 Tolerance: 15.0 ppm, and Fragment Mass Error Tolerance: 0.5 Da. Protein and peptide signals
587 were selected using a <1% false discovery rate filter.

588

589 **cDNA library generation and RNA sequencing**

590 Library preparation and sequencing were performed at Ecole normale supérieure Génomique
591 ENS core facility (Paris, France). cDNAs were synthesized using a combination of random
592 primers and oligodT to amplify RNAs independently of their polyadenylation status. 2 ng of total
593 RNA were amplified and converted to cDNA using NuGEN's Ovation RNA-Seq kit. Following
594 amplification, libraries were generated using the NexteraXT kit from Illumina. Libraries were
595 multiplexed, and after single-end 75 bp sequencing (NextSeq 500, Illumina), 40 to 60 million reads
596 per sample passed the Illumina filters. Three replicates per fraction and per cell cycle phase were
597 made, for a total of 24 libraries.

598

599 **RNA-seq analysis**

600 RNA-seq analysis was performed on a local Galaxy server. RNA STAR[70,71] (version 2.7.8a) was
601 used to align reads to the GRCh38p.13 assembly of the human genome with haplotypic
602 duplications removed. The following parameters were used: 2 maximum mismatches per read
603 alignment, a maximum ratio of mismatches to mapped length of 0.3, a minimum alignment score,
604 normalized to read length of 0.66. All other parameters were set to default. More than 95% of
605 reads mapped to the human genome, with the rest too short to be mapped. FeatureCounts[72]
606 (version 2.0.1) was used to count read using the Gencode v38 gene annotation. All parameters

607 were set to default. Differential expression analysis was done using DEseq2 with the default
608 settings. Normalized counts showed high reproducibility between replicates in both the PB and
609 pre-sorting fractions across the cell cycle (Figure S7), after exclusion of one PB replicate in G1S
610 and one pre-sorting replicate in mid G1, due to lower reproducibility (R<0.9). Depending on the
611 analysis, two normalizations were performed. (i) For PB enrichment calculation, PB replicates
612 were normalized to pre-sorting replicates within each cell cycle phase, as performed previously[7];
613 (ii) to follow the evolution of RNA content in the PB and pre-sorting fractions across the cell cycle,
614 all PB replicates were normalized together on the one hand, and all pre-sorting replicates together
615 on the other hand. It can be noted that PB enlargement throughout interphase may lead to some
616 underestimation of RNA content in PBs, since large PBs likely accumulate a larger pool of RNAs,
617 while RNA-seq only measures relative RNA abundance.

618

619 **Gene ontology analysis**

620 GO term analyses were performed using clusterProfiler[73,74] in R. For GO analysis of PB mRNAs
621 (Figure 2E): the reference list was a compilation of all mRNAs detected (normalized counts>0) in
622 the PB fraction of at least one cell cycle phase, and the test lists contained mRNAs displaying
623 differential abundance in the PB fraction (p-adj<0.05, DEseq2) between 2 cell cycle phases.
624 Similarly, for GO analysis of the pre-sorted fraction mRNAs (Figure S5B, C), the reference list
625 was a compilation of all mRNAs detected (normalized counts>0) in this fraction and the test lists
626 contained the mRNAs differentially expressed (p-adj<0.05, DEseq2). The Benjamini & Hochberg
627 p-value adjustment method was applied and the significance cutoff was set to <0.05. To limit GO
628 term redundancy, simplified GO terms were used with a cutoff of 0.6 using the adjusted p-value,
629 in Figure 2E. Dot plots were used to represent the top 10 GO categories with associated mRNAs
630 count and p-adj values. Full detailed GO term lists are provided in Supplementary Table 5.

631

632 **Immunofluorescence**

633 Cells grown on 22x22 mm glass coverslips were fixed for 20 min at room temperature (25°C) with
634 4% PFA (Electron Microscopy Sciences) diluted in PBS and stored at 4°C. Before IF labeling,
635 cells were permeabilized with 0.1% Triton X-100 in PBS (Sigma-Aldrich) for 15 min at room
636 temperature (25°C). To label DDX6, we used a rabbit polyclonal anti-DDX6 antibody recognizing
637 its C-ter extremity (BIOTECHNE, NB200-192) diluted 1/1000 in PBS, coupled to a secondary

638 F(ab)2 goat anti-rabbit antibody labeled with AF488 (Life technologies, A1107) diluted 1/1000 in
639 PBS. To label the stress granule marker TIA1, we used goat polyclonal anti-TIA1 antibody (Santa
640 Cruz, SC1751) diluted 1/200 in PBS, coupled to a secondary donkey anti-goat antibody labeled
641 with Cy3 (Jackson ImmunoResearch, 705-166-147) diluted 1/800 in PBS. All primary and
642 secondary antibodies were incubated for 1 hr at room temperature after which coverslips were
643 washed 3 times in PBS. Coverslips were then mounted using DAPI-containing Vectashield
644 (Vector Laboratories, Inc.).

645

646 **Single molecule FISH**

647 Cells grown on 22x22 mm glass coverslips were fixed for 20 min at room temperature with 4%
648 PFA (Electron Microscopy Sciences) diluted in PBS and permeabilized with 70% ethanol
649 overnight at 4°C. We used the single molecule inexpensive variant of smFISH (smiFISH)[33], which
650 uses 24 primary probes for each RNA target each made of a gene-specific sequence that
651 hybridizes to the RNA, and a common overhang that serve as platforms for recruiting fluorescently
652 labeled oligos (either Cy3 or Cy5). To this end, 40 pmoles of primary probes were first pre-
653 hybridized to 50 pmoles of fluorescently labeled oligos in 10 µL of 100 mM NaCl, 50 mM Tris-HCl,
654 10 mM $MgCl_2$, pH 7.9. This was performed on a thermocycler with the following program: 85 °C
655 for 3 min, 65 °C for 3 min, and 25 °C for 5 min. The resulting fluorescent probe duplexes were
656 then used in a hybridization mixture consisting of: 1x SSC, 0.34 mg/mL tRNA, 15% formamide
657 (Sigma-Aldrich), 2 mM vanadyl ribonucleoside complexes (Sigma-Aldrich), 0.2 mg/mL RNase-
658 free bovine serum albumin (Roche Diagnostics), 10% Dextran sulfate (MP Biomedicals), and 2
659 µL fluorescent duplexes per 100 µl hybridization volume. Hybridization was performed overnight
660 at 37°C. The next day, coverslips were washed in a 15% formamide 1x SSC solution for 40 min
661 twice. Coverslips were then mounted using DAPI-containing Vectashield (Vector Laboratories,
662 Inc.). All probe sequence are available in Supplementary Table 6.

663

664 **High-throughput smFISH**

665 HT-smFISH was performed as described previously[75]. Probesets against mRNAs of interest were
666 generated starting from a pool of DNA oligonucleotides (GenScript). The design of DNA
667 oligonucleotides was based on the Oligostan script[33]. Briefly, oligos belonging to the same
668 probeset (hybridizing to the same mRNA target) share a common barcode which allows their

669 specific amplification through 2 rounds of PCR. Then, *in-vitro* transcription is used to generate
670 transcript-specific primary RNA probesets. Each primary RNA probe contains a hybridization
671 sequence recognizing the target of interest, flanked by 2 readout sequences. These readout
672 sequences serve as platforms to recruit fluorescent TYE-563-labeled locked nuclei acids (similar
673 to the smiFISH technique[33]). For each mRNA target, 25 ng of each of the fluorescent locked nuclei
674 acids were prehybridized with 50 ng of primary RNA probeset in 100 µL of a solution containing
675 7.5 M urea (Sigma-Aldrich), 0.34 mg/mL tRNA, and 10% Dextran sulfate. Pre-hybridization was
676 done using thermocycler with the following program: 90°C for 3 min, 53°C for 15 min, giving rise
677 to fluorescent duplexes. Cells were grown in 96-well plates with glass bottoms, fixed with 4% PFA
678 for 20 min, and permeabilized with 70% ethanol overnight. Cells were then washed with PBS and
679 hybridization buffer (1× SSC, 7.5 M urea), and the 100 µL solution containing fluorescent duplexes
680 was added. Cells were incubated at 48 °C overnight. The next morning, plates were washed 8
681 times for 20 min each in 1× SSC, and 7.5 M urea at 48 °C. Finally, cells were washed with PBs,
682 labeled with DAPI at 5 µg/mL, and mounted in 90% glycerol (VWR), 1 mg/mL p-Phenylenediamine
683 (Sigma-Aldrich) and PBS pH 8.

684

685 **Imaging**

686 smFISH and IF imaging were performed using an inverted Zeiss Z1 widefield fluorescence
687 microscope equipped with a motorized stage. A 63x oil objective with a numerical aperture of 1.4
688 and an Axiocam 506 mono camera (Zeiss) with a pixel size of 72 nm were used. The microscope
689 was controlled by the Zeiss ZEN blue software (version 3.5.093.00003). Z stacks were acquired
690 with a 0.3 µm spacing between each plane. This spacing provided adequate single molecule
691 detection without oversampling. Maximum intensity projection (MIP) was used to obtain 2D
692 images for visualization, mounting, and analysis. The following exposure duration and laser
693 powers were used: 300-500 ms exposure at 100% laser power to image RNA in the Cy3 or Cy5
694 channels and PBs labeled with anti-DDX6 in the GFP channel; 50 ms at 50% laser power to image
695 GFP-LSM14A-labeled PBs in the GFP channel and DNA in the DAPI channel. For the HT-smFISH
696 screen, 96-well plates were imaged on an Opera Phenix High-Content Screening System
697 (PerkinElmer), with a 63× water-immersion objective (NA 1.15). Three-dimensional images were
698 acquired, with a spacing of 0.3 µm. Figures were mounted using ImageJ, Adobe illustrator, and
699 the OMERO Figure tool[76].

700

701 **Image analysis**

702 To analyze PB characteristics in HEK293-FUCCI cells, nuclei and cell segmentation was done
703 using the Cellpose[77] model with watershed. Nuclei were segmented using the DAPI channel, and
704 the cytoplasm using the DDX6 immunofluorescence channel using an intensity threshold of 350-
705 450. To determine the cell cycle phase based on the nuclear FUCCI signal, we used the Otsu
706 method to classify nuclei as positive or negative in the green and red channels. All images were
707 inspected to verify the reliability of the classification. PBs were detected based on DDX6
708 immunofluorescence using the BigFISH[78] Segmentation subpackage applied to the cytoplasm,
709 and PB GFP masks were generated based on a fluorescence intensity threshold of 1200-1500.
710 PBs were then assigned to individual cells and the mean PB fluorescence intensity was
711 computed. The fluorescence background (250), estimated from areas of the image without cells,
712 was subtracted from PB intensity values. PB size was computed as the maximal rectangular
713 perimeter occupied by a PB, multiplied by the pixel size (72 nm) and divided by 2. PBs with size
714 appearing smaller than 200 nm were excluded as they approach the diffraction limit of the
715 microscope in the green channel. Images from 2 independent experiments were normalized to
716 have the same PB intensity distribution means. The few PBs overlapping the nucleus in the MIPs
717 were not taken into consideration.

718 smFISH images were analysed using BigFISH[78], a python implementation of FISH-quant[79]
719 available at https://github.com/fish-quant/big-fish. The specific code used to analyze RNA
720 localization in PBs is available at https://github.com/15bonte/p_bodies_cycle_2023. Nuclei and
721 cell segmentation was done using the Cellpose[77] model with watershed. Nuclei were segmented
722 using the DAPI channel. The cytoplasm was segmented using background from the smFISH
723 channel using an intensity threshold of 400-500. Spot detection was done using the Detection
724 subpackage of BigFISH, which uses a Laplacian of Gaussian filter to enhance the spot signal. A
725 local maximal algorithm then localizes every peak in the image, and a threshold was applied to
726 discriminate the actual spots from the nonspecific background signal. One advantage BigFISH
727 provides is the ability to automatically set an optimal RNA spot detection threshold regardless of
728 the signal-to-background ratio of the smFISH. This parameter-free detection was used for all
729 RNAs imaged in this study and manually adjusted when needed to obtain a unimodal distribution
730 of single molecule fluorescence intensities. Next, we decomposed dense areas of RNA signal,
731 firstly by removing background noise with a Gaussian background subtraction and secondly using
732 the cluster decomposition tool. This tool computes the median detected spot intensity distribution,
733 fits it with a Gaussian distribution signal, and uses it to compute the number of spots that best fit

734 within each cluster. Next we detected PBs as masks using the GFP channel and the BigFISH
735 Segmentation subpackage with a fluorescence intensity threshold of 2200 for cells synchronized
736 in G1S, mid S and G2M, and 1600 for cells synchronized in mid G1, since PBs were less bright.
737 We then computed two RNA populations: (i) RNA molecules in the cytoplasm (i.e. outside the
738 nucleus), (ii) and RNA molecules in PBs (i.e. within the GFP mask). Since BigFISH was applied
739 to MIPs, some PBs overlapped with the nucleus in a minority of cells and were excluded from the
740 analysis. Cells without labeled PBs, with improper segmentation, or incomplete cell fragments
741 were also excluded. In experiments involving transient transfection (Figure 7, Renilla Luciferase
742 reporters), cells with fewer than 15 mRNA molecules (2 cells) or with too high expression for
743 proper BigFISH detection (2 cells) were excluded.

744 For HT-smFISH analysis, a similar BigFISH pipeline was used to segment cells, nuclei
745 and detect RNA spots. The specific code used to analyze HT-smFISH images is available here:
746 https://github.com/Flo3333/Cell-cycle-and-HT-smFISH-analysis-of-RNA-localization-in-PBs. PBs
747 were detected as 2D mask using a log filter (sigma = 2.25) to detect PB edges from the average
748 projection of the image stack. A threshold was then applied to segment PBs edges by detecting
749 positive grandients of intensity on the filtered image. Finally, PBs masks were filled and artifacts
750 smaller than 10 pixels are removed. Cells without labeled PBs or RNA spot, with improper
751 segmentation, and incomplete cells were excluded from the image analysis. To classify cells in
752 G1 or G2, we first calculated the integrated DAPI signal in each nucleus (nucleus area multiplied
753 by the mean DAPI signal). The obtained profile was then fitted, using a ranking-based
754 classification, to a cell cycle profile of HEK293 cells expressing GFP-LSM14A obtained with flow
755 cytometry and analyzed using the Dean-Jett model (~50% cells in G1 and ~16.5% of cells in G2).

756

757 **Western blots**

758 Cytoplasmic proteins were extracted as described previously[80], separated on a NuPage 4%–12%
759 gel (Invitrogen, Life Technologies) and transferred to Optitran BA-S83 nitrocellulose membrane
760 (GE healthcare life science). After blocking in PBS containing 5% (wt/vol) nonfat dry milk for 1 hr
761 at room temperature, membranes were incubated with the primary antibody overnight at 4°C,
762 washed in PBS, and incubated with horseradish peroxidase–conjugated secondary antibody
763 diluted 1/10,000 for 1 hr at room temperature. Primary antibodies were: rabbit anti-DDX6 (Bethyl,
764 Cat#BL2142, diluted 1/15,000), rabbit anti-4E-T (Abcam, Cat#ab95030, 1/2,500), rabbit anti-
765 LSM14A (Bethyl, Cat#A305-102A, 1/5,000), rabbit anti-PAT1b (Cell Signaling, Cat#14288S,

766 1/1,000), and rabbit anti- rProt S6 (5G10, Cell signaling, Cat#2217, 1/5,000). After washing in
767 PBS, proteins were detected using the Western lightning plus ECL kit (Perkin Elmer) and
768 visualized by exposure to CL-XPosure film (Pierce).

769

770 **Statistical analysis**

771 Boxplot representations and statistical tests were performed using the GraphPad Prism software
772 (GraphPad software v8, Inc), the R suite (v 4.2.0, https://www.R-project.org, R Core Team 2018.
773 R: A language and environment for statistical computing. R Foundation for Statistical Computing,
774 Vienna, Austria), and R studio (v 2022.12.0). Other graphical representations were generated
775 using Excel 2016 and the Excel Analysis ToolPak (Microsoft).

**Acknowledgments**: A.S., E.C. and A.L. were supported by the Agence Nationale pour la Recherche (ANR), grant number ANR-19-CE12-0024-01. The work was supported by the Association pour la Recherche sur le Cancer (PJA20181208011) to D.W., ANR grant ANR-19-CE12-0024 to D.W., D.G. and E.B. and MSDAvenir to E.B., and by the France Génomique national infrastructure, funded as part of the "Investissements d'Avenir" program managed by the ANR (contract ANR-10-INBS-0009). We thank Nancy Standart (University of Cambridge, UK) for critical reading of the manuscript, Zoher Gueroui (École normale supérieure Paris, France) for scientific discussions, and Vincent Galy (IBPS, Paris, France) for his contribution to the Zeiss microscope.

**Author contributions:** Conceptualization, A.S. and D.W.; Formal Analysis, A.S., M-N.B., F.S., M.K., A.L. and D.W.; Funding Acquisition, D.W.; Investigation, A.S., M-N.B., M.E.-L., E.C., A.M.G., A.V., C.B. and G.C.; Project Administration, D.W.; Software, T.B. and A.I.; Supervision, A.S., E.B., D.G., T.W., M.B. and D.W.; Validation, A.S., M-N.B., O.P., M.E.-L. and D.W.; Visualization, A.S., M-N.B. and M.K.; Writing – Original Draft, A.S. and D.W. All authors discussed the results and commented on the manuscript.

**Competing interests:** The authors declare no competing interests.

794 **References**


795 1. Lyon, A.S., Peeples, W.B., and Rosen, M.K. (2021). A framework for understanding the functions of
796 biomolecular condensates across scales. Nat Rev Mol Cell Biol *22*, 215–235. 10.1038/s41580-020-
797 00303-z.

798 2. Antifeeva, I.A., Fonin, A.V., Fefilova, A.S., Stepanenko, O.V., Povarova, O.I., Silonov, S.A., Kuznetsova,
799 I.M., Uversky, V.N., and Turoverov, K.K. (2022). Liquid-liquid phase separation as an organizing
800 principle of intracellular space: overview of the evolution of the cell compartmentalization concept.
801 Cell Mol Life Sci *79*, 251. 10.1007/s00018-022-04276-4.

802 3. Hirose, T., Ninomiya, K., Nakagawa, S., and Yamazaki, T. (2022). A guide to membraneless organelles
803 and their various roles in gene regulation. Nat Rev Mol Cell Biol, 1–17. 10.1038/s41580-022-00558-8.

804 4. Woodruff, J.B., Hyman, A.A., and Boke, E. (2018). Organization and Function of Non-dynamic
805 Biomolecular Condensates. Trends in Biochemical Sciences *43*, 81–94. 10.1016/j.tibs.2017.11.005.

806 5. Bhat, P., Honson, D., and Guttman, M. (2021). Nuclear compartmentalization as a mechanism of
807 quantitative control of gene expression. Nat Rev Mol Cell Biol *22*, 653–670. 10.1038/s41580-021-
808 00387-1.

809 6. Standart, N., and Weil, D. (2018). P-Bodies: Cytosolic Droplets for Coordinated mRNA Storage. Trends
810 Genet. *34*, 612–626. 10.1016/j.tig.2018.05.005.

811 7. Hubstenberger, A., Courel, M., Bénard, M., Souquere, S., Ernoult-Lange, M., Chouaib, R., Yi, Z.,
812 Morlot, J.-B., Munier, A., Fradet, M., et al. (2017). P-Body Purification Reveals the Condensation of
813 Repressed mRNA Regulons. Mol. Cell *68*, 144-157.e5. 10.1016/j.molcel.2017.09.003.

814 8. Courel, M., Clément, Y., Bossevain, C., Foretek, D., Vidal Cruchez, O., Yi, Z., Bénard, M., Benassy, M.-
815 N., Kress, M., Vindry, C., et al. (2019). GC content shapes mRNA storage and decay in human cells.
816 eLife *8*, e49708. 10.7554/eLife.49708.

817 9. Pillai, R.S., Bhattacharyya, S.N., Artus, C.G., Zoller, T., Cougot, N., Basyuk, E., Bertrand, E., and
818 Filipowicz, W. (2005). Inhibition of Translational Initiation by Let-7 MicroRNA in Human Cells. Science
819 *309*, 1573–1576. 10.1126/science.1115079.

820 10. Pitchiaya, S., Mourao, M.D.A., Jalihal, A.P., Xiao, L., Jiang, X., Chinnaiyan, A.M., Schnell, S., and
821 Walter, N.G. (2019). Dynamic Recruitment of Single RNAs to Processing Bodies Depends on RNA
822 Functionality. Molecular Cell *74*, 521-533.e6. 10.1016/j.molcel.2019.03.001.

823 11. Bhattacharyya, S.N., Habermacher, R., Martine, U., Closs, E.I., and Filipowicz, W. (2006). Relief of
824 microRNA-Mediated Translational Repression in Human Cells Subjected to Stress. Cell *125*, 1111–
825 1124. 10.1016/j.cell.2006.04.031.

826 12. Aizer, A., Kalo, A., Kafri, P., Shraga, A., Ben-Yishay, R., Jacob, A., Kinor, N., and Shav-Tal, Y. (2014).
827 Quantifying mRNA targeting to P-bodies in living human cells reveals their dual role in mRNA decay
828 and storage. J Cell Sci *127*, 4443–4456. 10.1242/jcs.152975.

829 13. Cho, C.-Y., Kelliher, C.M., and Haase, S.B. (2019). The cell-cycle transcriptional network
830 generates and transmits a pulse of transcription once each cell cycle. Cell Cycle *18*, 363–378.
831 10.1080/15384101.2019.1570655.

832 14. Sun, Q., Jiao, F., Lin, G., Yu, J., and Tang, M. (2019). The nonlinear dynamics and fluctuations of
833 mRNA levels in cell cycle coupled transcription. PLOS Computational Biology *15*, e1007017.
834 10.1371/journal.pcbi.1007017.

835 15. Bristow, S.L., Leman, A.R., and Haase, S.B. (2014). Cell Cycle-Regulated Transcription: Effectively
836 Using a Genomics Toolbox. Cell Cycle Control *1170*, 3–27. 10.1007/978-1-4939-0888-2_1.

837 16. Liu, Y., Chen, S., Wang, S., Soares, F., Fischer, M., Meng, F., Du, Z., Lin, C., Meyer, C., DeCaprio,
838 J.A., et al. (2017). Transcriptional landscape of the human cell cycle. Proceedings of the National
839 Academy of Sciences *114*, 3473–3478. 10.1073/pnas.1617636114.

840 17. Fischer, M., Schade, A.E., Branigan, T.B., Müller, G.A., and DeCaprio, J.A. (2022). Coordinating
841 gene expression during the cell cycle. Trends in Biochemical Sciences *47*, 1009–1022.
842 10.1016/j.tibs.2022.06.007.

843 18. Bertoli, C., Skotheim, J.M., and de Bruin, R.A.M. (2013). Control of cell cycle transcription during
844 G1 and S phases. Nat Rev Mol Cell Biol *14*, 518–528. 10.1038/nrm3629.

845 19. Eser, P., Demel, C., Maier, K.C., Schwalb, B., Pirkl, N., Martin, D.E., Cramer, P., and Tresch, A.
846 (2014). Periodic mRNA synthesis and degradation co-operate during cell cycle gene expression.
847 Molecular Systems Biology *10*, 717. 10.1002/msb.134886.

848 20. Chávez, S., García-Martínez, J., Delgado-Ramos, L., and Pérez-Ortín, J.E. (2016). The importance
849 of controlling mRNA turnover during cell proliferation. Curr Genet *62*, 701–710. 10.1007/s00294-016-
850 0594-2.

851 21. Catala, M., and Abou Elela, S. (2019). Promoter-dependent nuclear RNA degradation ensures cell
852 cycle-specific gene expression. Commun Biol *2*, 1–13. 10.1038/s42003-019-0441-3.

853 22. Krenning, L., Sonneveld, S., and Tanenbaum, M.E. (2022). Time-resolved single-cell sequencing
854 identifies multiple waves of mRNA decay during the mitosis-to-G1 phase transition. eLife *11*, e71356.
855 10.7554/eLife.71356.

856 23. Battich, N., Beumer, J., de Barbanson, B., Krenning, L., Baron, C.S., Tanenbaum, M.E., Clevers, H.,
857 and van Oudenaarden, A. (2020). Sequencing metabolically labeled transcripts in single cells reveals
858 mRNA turnover strategies. Science *367*, 1151–1156. 10.1126/science.aax3072.

859 24. Gingold, H., Tehler, D., Christoffersen, N.R., Nielsen, M.M., Asmar, F., Kooistra, S.M.,
860 Christophersen, N.S., Christensen, L.L., Borre, M., Sørensen, K.D., et al. (2014). A dual program for
861 translation regulation in cellular proliferation and differentiation. Cell *158*, 1281–1292.
862 10.1016/j.cell.2014.08.011.

863 25. Yang, Z., Jakymiw, A., Wood, M.R., Eystathioy, T., Rubin, R.L., Fritzler, M.J., and Chan, E.K.L.
864 (2004). GW182 is critical for the stability of GW bodies expressed during the cell cycle and cell
865 proliferation. Journal of Cell Science *117*, 5567–5578. 10.1242/jcs.01477.

866 26. Grant, G.D., Kedziora, K.M., Limas, J.C., Cook, J.G., and Purvis, J.E. (2018). Accurate delineation
867 of cell cycle phase transitions in living cells with PIP-FUCCI. Cell Cycle *17*, 2496–2516.
868 10.1080/15384101.2018.1547001.

869 27. Sakaue-Sawano, A., Kurokawa, H., Morimura, T., Hanyu, A., Hama, H., Osawa, H., Kashiwagi, S.,
870 Fukami, K., Miyata, T., Miyoshi, H., et al. (2008). Visualizing spatiotemporal dynamics of multicellular
871 cell-cycle progression. Cell *132*, 487–498. 10.1016/j.cell.2007.12.033.

872 28. Ayache, J., Bénard, M., Ernoult-Lange, M., Minshall, N., Standart, N., Kress, M., and Weil, D.
873 (2015). P-body assembly requires DDX6 repression complexes rather than decay or Ataxin2/2L
874 complexes. MBoC *26*, 2579–2595. 10.1091/mbc.E15-03-0136.

875 29. Vassilev, L.T., Tovar, C., Chen, S., Knezevic, D., Zhao, X., Sun, H., Heimbrook, D.C., and Chen, L.
876 (2006). Selective small-molecule inhibitor reveals critical mitotic functions of human CDK1.
877 Proceedings of the National Academy of Sciences *103*, 10660–10665. 10.1073/pnas.0600447103.

878 30. Dominguez, D., Tsai, Y.-H., Gomez, N., Jha, D.K., Davis, I., and Wang, Z. (2016). A high-resolution
879 transcriptome map of cell cycle reveals novel connections between periodic genes and cancer. Cell
880 Res *26*, 946–962. 10.1038/cr.2016.84.

881 31. Love, M.I., Huber, W., and Anders, S. (2014). Moderated estimation of fold change and
882 dispersion for RNA-seq data with DESeq2. Genome Biol *15*, 1–21. 10.1186/s13059-014-0550-8.

883 32. Femino, A.M., Fay, F.S., Fogarty, K., and Singer, R.H. (1998). Visualization of Single RNA
884 Transcripts in Situ. Science *280*, 585–590. 10.1126/science.280.5363.585.

885 33. Tsanov, N., Samacoits, A., Chouaib, R., Traboulsi, A.-M., Gostan, T., Weber, C., Zimmer, C.,
886 Zibara, K., Walter, T., Peter, M., et al. (2016). smiFISH and FISH-quant - a flexible single RNA detection
887 approach with super-resolution capability. Nucleic Acids Res. *44*, e165. 10.1093/nar/gkw784.

888 34. Cappell, S.D., Mark, K.G., Garbett, D., Pack, L.R., Rape, M., and Meyer, T. (2018). EMI1 switches
889 from being a substrate to an inhibitor of APC/CCDH1 to start the cell cycle. Nature *558*, 313–317.
890 10.1038/s41586-018-0199-7.

891 35. Reimann, J.D., Gardner, B.E., Margottin-Goguet, F., and Jackson, P.K. (2001). Emi1 regulates the
892 anaphase-promoting complex by a different mechanism than Mad2 proteins. Genes Dev *15*, 3278–
893 3285. 10.1101/gad.945701.

894 36. Machida, Y.J., and Dutta, A. (2007). The APC/C inhibitor, Emi1, is essential for prevention of
895 rereplication. Genes Dev *21*, 184–194. 10.1101/gad.1495007.

896 37. Reimann, J.D., Freed, E., Hsu, J.Y., Kramer, E.R., Peters, J.M., and Jackson, P.K. (2001). Emi1 is a
897 mitotic regulator that interacts with Cdc20 and inhibits the anaphase promoting complex. Cell *105*,
898 645–655. 10.1016/s0092-8674(01)00361-0.

899 38. Miller, J.J., Summers, M.K., Hansen, D.V., Nachury, M.V., Lehman, N.L., Loktev, A., and Jackson,
900 P.K. (2006). Emi1 stably binds and inhibits the anaphase-promoting complex/cyclosome as a
901 pseudosubstrate inhibitor. Genes Dev *20*, 2410–2420. 10.1101/gad.1454006.

902 39. Di Fiore, B., and Pines, J. (2007). Emi1 is needed to couple DNA replication with mitosis but does
903 not regulate activation of the mitotic APC/C. Journal of Cell Biology *177*, 425–437.
904 10.1083/jcb.200611166.

905 40. Hsu, J.Y., Reimann, J.D.R., Sørensen, C.S., Lukas, J., and Jackson, P.K. (2002). E2F-dependent
906 accumulation of hEmi1 regulates S phase entry by inhibiting APC(Cdh1). Nat Cell Biol *4*, 358–366.
907 10.1038/ncb785.

908 41. Dominguez, D., Tsai, Y.-H., Weatheritt, R., Wang, Y., Blencowe, B.J., and Wang, Z. (2016). An
909 extensive program of periodic alternative splicing linked to cell cycle progression. eLife *5*, e10288.
910 10.7554/eLife.10288.

911 42. Nielsen, C.F., Zhang, T., Barisic, M., Kalitsis, P., and Hudson, D.F. (2020). Topoisomerase IIα is
912 essential for maintenance of mitotic chromosome structure. Proc Natl Acad Sci U S A *117*, 12131–
913 12142. 10.1073/pnas.2001760117.

914 43. Lee, S., Jung, S.-R., Heo, K., Byl, J.A.W., Deweese, J.E., Osheroff, N., and Hohng, S. (2012). DNA
915 cleavage and opening reactions of human topoisomerase IIα are regulated via Mg2+-mediated
916 dynamic bending of gate-DNA. Proc Natl Acad Sci U S A *109*, 2925–2930. 10.1073/pnas.1115704109.

917 44. Roca, J. (2009). Topoisomerase II: a fitted mechanism for the chromatin landscape. Nucleic Acids
918 Res *37*, 721–730. 10.1093/nar/gkn994.

919 45. Heck, M.M., Hittelman, W.N., and Earnshaw, W.C. (1988). Differential expression of DNA
920 topoisomerases I and II during the eukaryotic cell cycle. Proc Natl Acad Sci U S A *85*, 1086–1090.
921 10.1073/pnas.85.4.1086.

922 46. Woessner, R.D., Mattern, M.R., Mirabelli, C.K., Johnson, R.K., and Drake, F.H. (1991).
923 Proliferation- and cell cycle-dependent differences in expression of the 170 kilodalton and 180
924 kilodalton forms of topoisomerase II in NIH-3T3 cells. Cell Growth Differ *2*, 209–214.

925 47. Kimura, K., Saijo, M., Ui, M., and Enomoto, T. (1994). Growth state- and cell cycle-dependent
926 fluctuation in the expression of two forms of DNA topoisomerase II and possible specific modification
927 of the higher molecular weight form in the M phase. J Biol Chem *269*, 1173–1176.

928 48. Lee, J.H., and Berger, J.M. (2019). Cell Cycle-Dependent Control and Roles of DNA
929 Topoisomerase II. Genes *10*. 10.3390/genes10110859.

930 49. Hopfner, R., Mousli, M., Jeltsch, J.M., Voulgaris, A., Lutz, Y., Marin, C., Bellocq, J.P., Oudet, P.,
931 and Bronner, C. (2000). ICBP90, a novel human CCAAT binding protein, involved in the regulation of
932 topoisomerase IIalpha expression. Cancer Res *60*, 121–128.

933 50. Magan, N., Szremska, A.P., Isaacs, R.J., and Stowell, K.M. (2003). Modulation of DNA
934 topoisomerase II alpha promoter activity by members of the Sp (specificity protein) and NF-Y (nuclear
935 factor Y) families of transcription factors. Biochem J *374*, 723–729. 10.1042/BJ20030032.

936 51. Liao, H., Winkfein, R.J., Mack, G., Rattner, J.B., and Yen, T.J. (1995). CENP-F is a protein of the
937 nuclear matrix that assembles onto kinetochores at late G2 and is rapidly degraded after mitosis. J
938 Cell Biol *130*, 507–518. 10.1083/jcb.130.3.507.

939 52. Yang, Z.Y., Guo, J., Li, N., Qian, M., Wang, S.N., and Zhu, X.L. (2003). Mitosin/CENP-F is a
940 conserved kinetochore protein subjected to cytoplasmic dynein-mediated poleward transport. Cell
941 Res *13*, 275–283. 10.1038/sj.cr.7290172.

942 53. Chan, G.K., Jablonski, S.A., Sudakin, V., Hittle, J.C., and Yen, T.J. (1999). Human BUBR1 is a
943 mitotic checkpoint kinase that monitors CENP-E functions at kinetochores and binds the
944 cyclosome/APC. J Cell Biol *146*, 941–954. 10.1083/jcb.146.5.941.

945 54. Shin, H.J., Baek, K.H., Jeon, A.H., Park, M.T., Lee, S.J., Kang, C.M., Lee, H.S., Yoo, S.H., Chung,
946 D.H., Sung, Y.C., et al. (2003). Dual roles of human BubR1, a mitotic checkpoint kinase, in the
947 monitoring of chromosomal instability. Cancer Cell *4*, 483–497. 10.1016/s1535-6108(03)00302-7.

948 55. Tatsumoto, T., Xie, X., Blumenthal, R., Okamoto, I., and Miki, T. (1999). Human Ect2 Is an
949 Exchange Factor for Rho Gtpases, Phosphorylated in G2/M Phases, and Involved in Cytokinesis.
950 Journal of Cell Biology *147*, 921–928. 10.1083/jcb.147.5.921.

951 56. Liu, X., and Winey, M. (2012). The MPS1 Family of Protein Kinases. Annu Rev Biochem *81*, 561–
952 585. 10.1146/annurev-biochem-061611-090435.

953 57. Zhang, Y., Tan, L., Yang, Q., Li, C., and Liou, Y.-C. (2018). The microtubule-associated protein
954 HURP recruits the centrosomal protein TACC3 to regulate K-fiber formation and support chromosome
955 congression. Journal of Biological Chemistry *293*, 15733–15747. 10.1074/jbc.RA118.003676.

956 58. Klosin, A., Oltsch, F., Harmon, T., Honigmann, A., Jülicher, F., Hyman, A.A., and Zechner, C.
957 (2020). Phase separation provides a mechanism to reduce noise in cells. Science *367*, 464–468.
958 10.1126/science.aav6691.

959 59. Azzam, M.E., and Algranati, I.D. (1973). Mechanism of Puromycin Action: Fate of Ribosomes
960 after Release of Nascent Protein Chains from Polysomes. Proc. Natl. Acad. Sci. U.S.A. *70*, 3866–3869.
961 10.1073/pnas.70.12.3866.

962 60. Chouaib, R., Safieddine, A., Pichon, X., Imbert, A., Kwon, O.S., Samacoits, A., Traboulsi, A.-M.,
963 Robert, M.-C., Tsanov, N., Coleno, E., et al. (2020). A Dual Protein-mRNA Localization Screen Reveals
964 Compartmentalized Translation and Widespread Co-translational RNA Targeting. Developmental Cell
965 *54*, 773-791.e5. 10.1016/j.devcel.2020.07.010.

966 61. Safieddine, A., Coleno, E., Salloum, S., Imbert, A., Traboulsi, A.-M., Kwon, O.S., Lionneton, F.,
967 Georget, V., Robert, M.-C., Gostan, T., et al. (2021). A choreography of centrosomal mRNAs reveals a
968 conserved localization mechanism involving active polysome transport. Nat Commun *12*, 1352.
969 10.1038/s41467-021-21585-7.

970 62. Frenkel-Morgenstern, M., Danon, T., Christian, T., Igarashi, T., Cohen, L., Hou, Y.-M., and Jensen,
971 L.J. (2012). Genes adopt non-optimal codon usage to generate cell cycle-dependent oscillations in
972 protein levels. Mol Syst Biol *8*, 572. 10.1038/msb.2012.3.

973 63. Tanenbaum, M.E., Stern-Ginossar, N., Weissman, J.S., and Vale, R.D. (2015). Regulation of mRNA
974 translation during mitosis. eLife *4*, e07957. 10.7554/eLife.07957.

975 64. Cardona, A.H., Ecsedi, S., Khier, M., Yi, Z., Bahri, A., Ouertani, A., Valero, F., Labrosse, M.,
976 Rouquet, S., Robert, S., et al. (2023). Self-demixing of mRNA copies buffers mRNA:mRNA and
977 mRNA:regulator stoichiometries. Cell *186*, 4310-4324.e23. 10.1016/j.cell.2023.08.018.

978 65. Riback, J.A., Zhu, L., Ferrolino, M.C., Tolbert, M., Mitrea, D.M., Sanders, D.W., Wei, M.-T.,
979 Kriwacki, R.W., and Brangwynne, C.P. (2020). Composition-dependent thermodynamics of
980 intracellular phase separation. Nature *581*, 209–214. 10.1038/s41586-020-2256-2.

981 66. Sanchez-Burgos, I., Herriott, L., Collepardo-Guevara, R., and Espinosa, J.R. (2023). Surfactants or
982 scaffolds? RNAs of different lengths exhibit heterogeneous distributions and play diverse roles in
983 RNA-protein condensates. Biophysical Journal. 10.1016/j.bpj.2023.03.006.

984 67. Sanchez-Burgos, I., Espinosa, J.R., Joseph, J.A., and Collepardo-Guevara, R. (2022). RNA length
985 has a non-trivial effect in the stability of biomolecular condensates formed by RNA-binding proteins.
986 PLOS Computational Biology *18*, e1009810. 10.1371/journal.pcbi.1009810.

987 68. Cochard, A., Garcia-Jove Navarro, M., Piroska, L., Kashida, S., Kress, M., Weil, D., and Gueroui, Z.
988 (2022). RNA at the surface of phase-separated condensates impacts their size and number.
989 Biophysical Journal *121*, 1675–1690. 10.1016/j.bpj.2022.03.032.

990 69. Khong, A., Matheny, T., Jain, S., Mitchell, S.F., Wheeler, J.R., and Parker, R. (2017). The Stress
991 Granule Transcriptome Reveals Principles of mRNA Accumulation in Stress Granules. Molecular Cell
992 *68*, 808-820.e5. 10.1016/j.molcel.2017.10.015.

993 70. Dobin, A., Davis, C.A., Schlesinger, F., Drenkow, J., Zaleski, C., Jha, S., Batut, P., Chaisson, M., and
994 Gingeras, T.R. (2013). STAR: ultrafast universal RNA-seq aligner. Bioinformatics *29*, 15–21.
995 10.1093/bioinformatics/bts635.

996 71. Goecks, J., Nekrutenko, A., and Taylor, J. (2010). Galaxy: a comprehensive approach for
997 supporting accessible, reproducible, and transparent computational research in the life sciences.
998 Genome Biol *11*, 1–13. 10.1186/gb-2010-11-8-r86.

999 72. Liao, Y., Smyth, G.K., and Shi, W. (2014). featureCounts: an efficient general purpose program
1000 for assigning sequence reads to genomic features. Bioinformatics *30*, 923–930.
1001 10.1093/bioinformatics/btt656.

1002 73. Wu, T., Hu, E., Xu, S., Chen, M., Guo, P., Dai, Z., Feng, T., Zhou, L., Tang, W., Zhan, L., et al.
1003 (2021). clusterProfiler 4.0: A universal enrichment tool for interpreting omics data. Innovation *2*.
1004 10.1016/j.xinn.2021.100141.

1005 74. Yu, G., Wang, L.-G., Han, Y., and He, Q.-Y. (2012). clusterProfiler: an R Package for Comparing
1006 Biological Themes Among Gene Clusters. OMICS: A Journal of Integrative Biology *16*, 284–287.
1007 10.1089/omi.2011.0118.

1008 75. Safieddine, A., Coleno, E., Lionneton, F., Traboulsi, A.-M., Salloum, S., Lecellier, C.-H., Gostan, T.,
1009 Georget, V., Hassen-Khodja, C., Imbert, A., et al. (2023). HT-smFISH: a cost-effective and flexible
1010 workflow for high-throughput single-molecule RNA imaging. Nat Protoc *18*, 157–187.
1011 10.1038/s41596-022-00750-2.

1012 76. Allan, C., Burel, J.-M., Moore, J., Blackburn, C., Linkert, M., Loynton, S., MacDonald, D., Moore,
1013 W.J., Neves, C., Patterson, A., et al. (2012). OMERO: flexible, model-driven data management for
1014 experimental biology. Nat Methods *9*, 245–253. 10.1038/nmeth.1896.

1015 77. Stringer, C., Wang, T., Michaelos, M., and Pachitariu, M. (2021). Cellpose: a generalist algorithm
1016 for cellular segmentation. Nat Methods *18*, 100–106. 10.1038/s41592-020-01018-x.

1017 78. Imbert, A., Ouyang, W., Safieddine, A., Coleno, E., Zimmer, C., Bertrand, E., Walter, T., and
1018 Mueller, F. (2022). FISH-quant v2: a scalable and modular tool for smFISH image analysis. RNA *28*,
1019 786–795. 10.1261/rna.079073.121.

1020 79. Mueller, F., Senecal, A., Tantale, K., Marie-Nelly, H., Ly, N., Collin, O., Basyuk, E., Bertrand, E.,
1021 Darzacq, X., and Zimmer, C. (2013). FISH-quant: automatic counting of transcripts in 3D FISH images.
1022 Nat. Methods *10*, 277–278. 10.1038/nmeth.2406.

1023 80. Balak, C., Benard, M., Schaefer, E., Iqbal, S., Ramsey, K., Ernoult-Lange, M., Mattioli, F., Llaci, L.,
1024 Geoffroy, V., Courel, M., et al. (2019). Rare De Novo Missense Variants in RNA Helicase DDX6 Cause
1025 Intellectual Disability and Dysmorphic Features and Lead to P-Body Defects and RNA Dysregulation.
1026 Am J Hum Genet *105*, 509–525. 10.1016/j.ajhg.2019.07.010.

1027

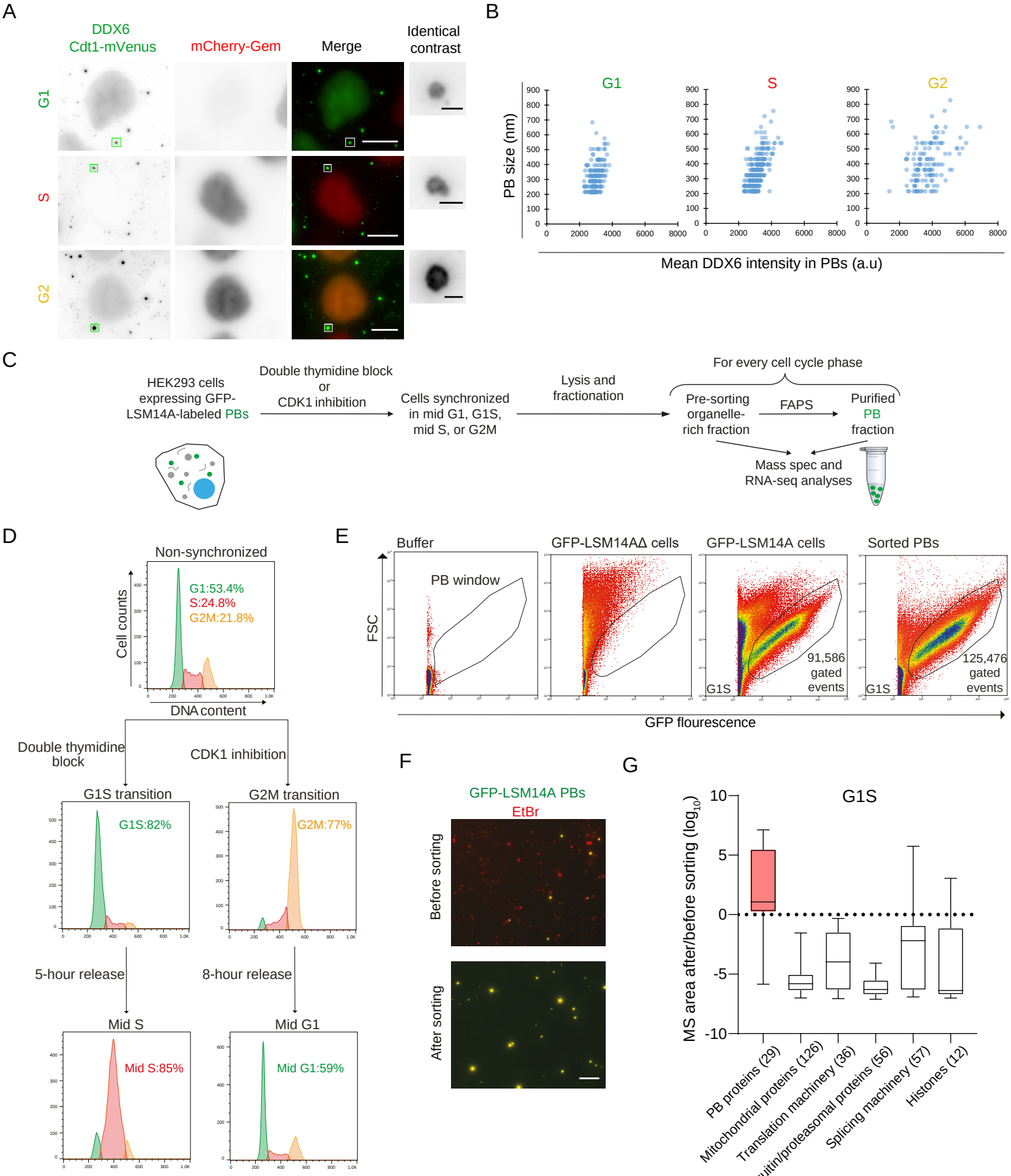
A
DDX6
Cdt1-mVenus
mCherry-Gem
Merge
Identical contrast
G1
S
G2
B
G1
S
G2
PB size (nm)
Mean DDX6 intensity in PBs (a.u)
C
HEK293 cells expressing GFP-LSM14A-labeled PBs
Double thymidine block or CDK1 inhibition
Cells synchronized in mid G1, G1S, mid S, or G2M
Lysis and fractionation
For every cell cycle phase
Pre-sorting organelle-rich fraction
FAPS
Purified PB fraction
Mass spec and RNA-seq analyses
D
Non-synchronized
Cell counts
G1:53.4%
S:24.8%
G2M:21.8%
DNA content
Double thymidine block
CDK1 inhibition
G1S transition
G1S:82%
G2M transition
G2M:77%
5-hour release
8-hour release
Mid S
Mid S:85%
Mid G1
Mid G1:59%
E
Buffer
GFP-LSM14AΔ cells
GFP-LSM14A cells
Sorted PBs
FSC
PB window
G1S
91,586 gated events
125,476 gated events
GFP flourescence
F
GFP-LSM14A PBs
EtBr
Before sorting
After sorting
G
G1S
MS area after/before sorting (log10)
PB proteins (29)
Mitochondrial proteins (126)
Translation machinery (36)
Ubiquitin/proteasomal proteins (56)
Splicing machinery (57)
Histones (12)
H
PB fractions
PB protein area in mid G1
PB protein area in G1S
PB protein area in mid S
PB protein area in G2M
LSM14A
MOV10
DDX6
IGF2BP1
EDC4
LSM14B
ILF3
APOBEC3F
MYH10
IGF2BP2
IGF2BP3
UPF1
DCP1A
4E-T
EDC3
PATL1
EIF4E

**Figure 1: PBs enlarge during cell cycle progression while maintaining a similar proteome.** (A) Widefield fluorescence images of HEK-FUCCI cells with DDX6-labeled PBs. Left panel: nuclear Cdt1-mVenus signal indicates cells in G1 or G2 phase, while cytoplasmic PBs were immunostained with anti-DDX6 antibodies (both in green in the merge). Middle panels: nuclear mCherry-Gem signal indicates cells in S or G2 phase (in red in the merge). Cell cycle phases are indicated on the left. Right insets present enlargements of a representative PB. Scale bars, 10 and 1 µm in the merge panels and insets, respectively. (B) Scatter plot representation of PB size and DDX6 intensity across the cell cycle (from 2 independent experiments). (C) Main steps of the FAPS procedure. (D) Cell cycle analysis from representative synchronized samples. The percentage of cells in the targeted cell cycle phase is displayed in each panel. (E) Representative FAPS profiles of pre-sorting lysate (middle-left panel) and sorted PBs (rightmost panel) from GFP-LSM14A cells synchronized at the G1S transition. Associated controls (buffer and lysate from GFP-LSM14Δ cells) are shown in left panels. The window used to sort PBs is outlined. (F) Representative widefield fluorescence images of lysates before and after sorting. PBs were labelled with GFP-LSM14A (in green) and contaminants were revealed by non-specific ethidium bromide (EtBr) staining (in red). Scale bar, 10 µm. (G) Boxplot showing the enrichment or depletion of several protein groups after sorting (ratio of MS area after/before sorting) in cells at the G1S transition. For each group, the number of detected proteins (protein area >1) is indicated in brackets. (H) Pairwise comparison of the abundance (MS area) of known PB proteins in the PB fraction between successive cell cycle stages.

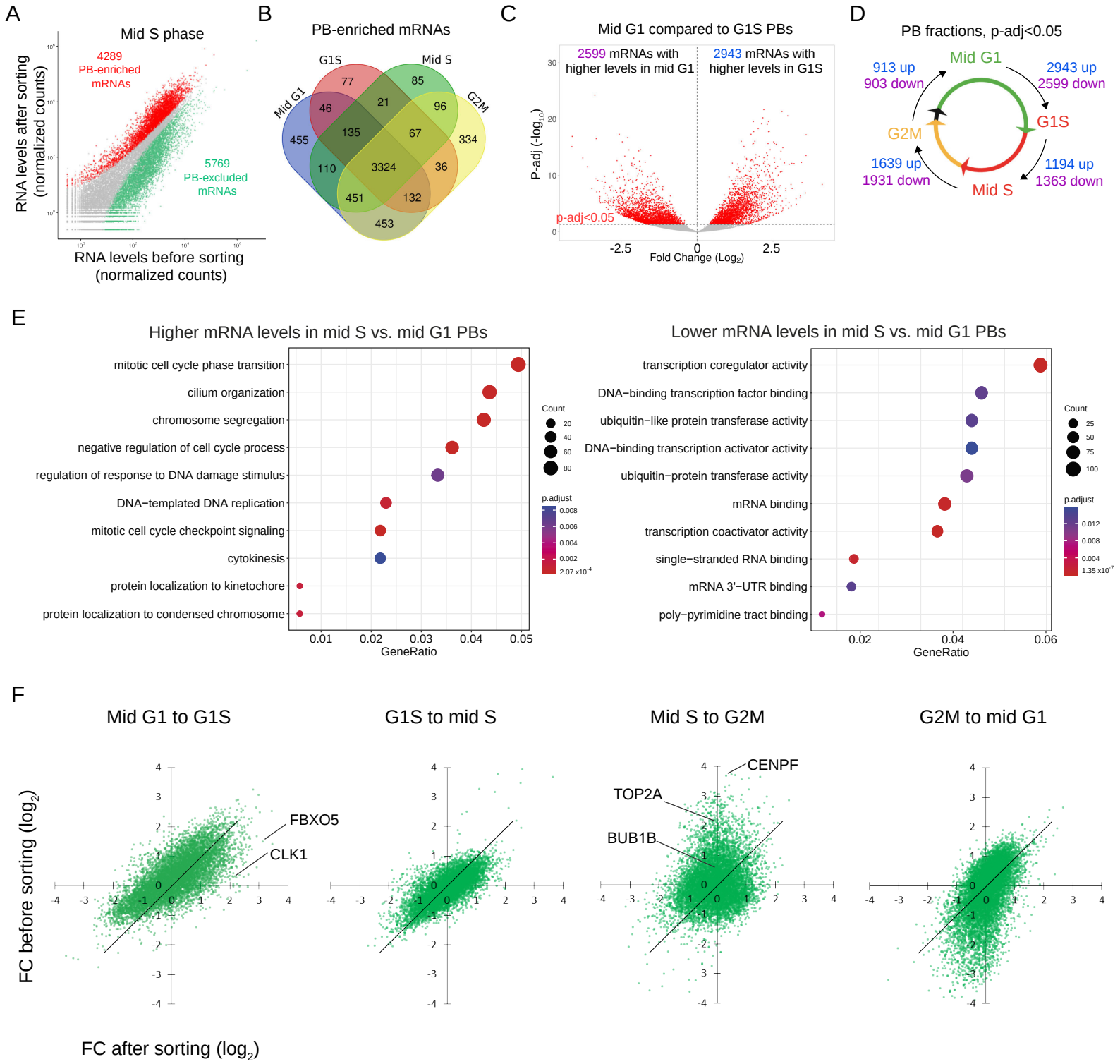
A
Mid S phase
4289
PB-enriched
mRNAs
5769
PB-excluded
mRNAs
RNA levels after sorting
(normalized counts)
RNA levels before sorting
(normalized counts)
B
PB-enriched mRNAs
G1S
Mid S
Mid G1
G2M
77
85
46
21
96
455
135
67
334
110
3324
36
451
132
453
C
Mid G1 compared to G1S PBs
2599 mRNAs with
higher levels in mid G1
2943 mRNAs with
higher levels in G1S
p-adj<0.05
P-adj (-log10)
Fold Change (Log2)
D
PB fractions, p-adj<0.05
Mid G1
913 up
903 down
2943 up
2599 down
G1S
G2M
1639 up
1931 down
1194 up
1363 down
Mid S
E
Higher mRNA levels in mid S vs. mid G1 PBs
mitotic cell cycle phase transition
cilium organization
chromosome segregation
negative regulation of cell cycle process
regulation of response to DNA damage stimulus
DNA−templated DNA replication
mitotic cell cycle checkpoint signaling
cytokinesis
protein localization to kinetochore
protein localization to condensed chromosome
GeneRatio
Count
p.adjust
Lower mRNA levels in mid S vs. mid G1 PBs
transcription coregulator activity
DNA−binding transcription factor binding
ubiquitin−like protein transferase activity
DNA−binding transcription activator activity
ubiquitin−protein transferase activity
mRNA binding
transcription coactivator activity
single−stranded RNA binding
mRNA 3'−UTR binding
poly−pyrimidine tract binding
GeneRatio
Count
p.adjust
F
Mid G1 to G1S
G1S to mid S
Mid S to G2M
G2M to mid G1
FBXO5
CLK1
CENPF
TOP2A
BUB1B
FC before sorting (log2)
FC after sorting (log2)

**Figure 2: Analysis of purified PBs uncovers their dynamic transcriptome**. (A) RNA levels (normalized DEseq2 counts) before and after PB sorting from mid S cells. Grey dots correspond to all expressed mRNAs (average counts >0). The mRNAs significantly enriched and depleted in PBs (p-adj<0.05) are shown in red and green, respectively. (B) Venn diagram showing the overlap between PB-enriched mRNAs in the different cell cycle phases. (C) Volcano plot showing the changes in PB mRNA content from mid S to G2M. Grey dots correspond to all expressed mRNAs (average counts >0). Significant changes (p-adj<0.05) are highlighted in red. Indicated mRNAs are further studied by smFISH. (D) Schematic summary of significant changes in PBs (p-adj<0.05) across the cell cycle. (E) GO analyses of PB mRNAs with significant changes in mid S compared to mid G1. The 10 most enriched GO categories are shown. The size of each dot represents the number of mRNAs within the GO category. The fraction of PB transcripts belonging to the category is on the x-axis (GeneRatio) and the significance of the enrichment is color-coded according to the right scale. (F) Quadrant plots comparing mRNA fold-changes before and after sorting (normalized counts >50) between successive cell cycle stages. Quadrant numbers and mRNAs further studied by smFISH are indicated. Volcano plots associated with these plots are in Figure S8.

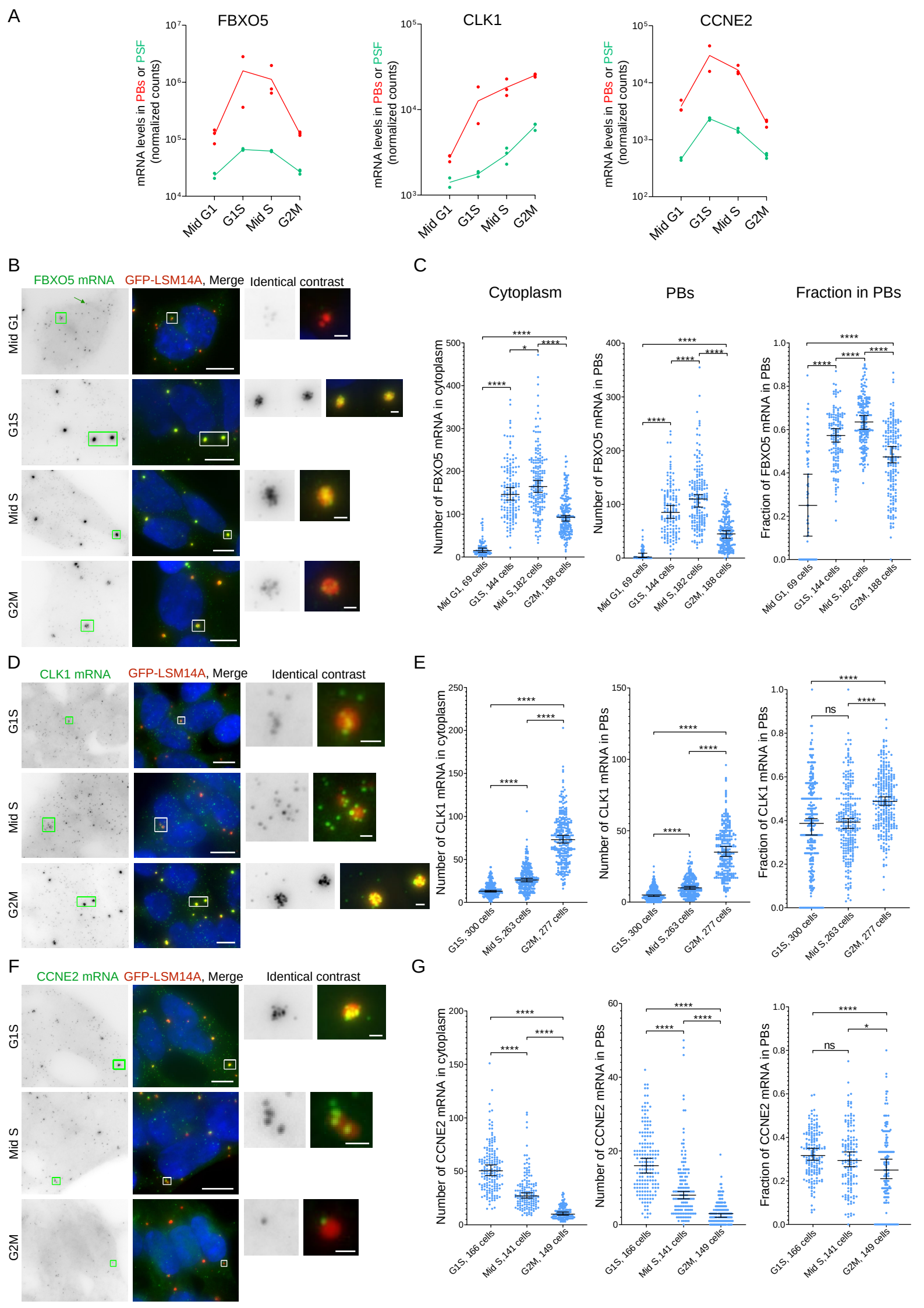
A
FBXO5
CLK1
CCNE2
mRNA levels in PBs or PSF (normalized counts)
Mid G1
G1S
Mid S
G2M
B
FBXO5 mRNA
GFP-LSM14A, Merge
Identical contrast
C
Cytoplasm
PBs
Fraction in PBs
Number of FBXO5 mRNA in cytoplasm
Number of FBXO5 mRNA in PBs
Fraction of FBXO5 mRNA in PBs
Mid G1, 69 cells
G1S, 144 cells
Mid S,182 cells
G2M, 188 cells
D
CLK1 mRNA
GFP-LSM14A, Merge
Identical contrast
E
Number of CLK1 mRNA in cytoplasm
Number of CLK1 mRNA in PBs
Fraction of CLK1 mRNA in PBs
G1S, 300 cells
Mid S,263 cells
G2M, 277 cells
F
CCNE2 mRNA
GFP-LSM14A, Merge
Identical contrast
G
Number of CCNE2 mRNA in cytoplasm
Number of CCNE2 mRNA in PBs
Fraction of CCNE2 mRNA in PBs
G1S, 166 cells
Mid S,141 cells
G2M, 149 cells

**Figure 3: mRNA localization in PBs can peak at any cell cycle phase.** (A) Evolution of FBXO5, CLK1, and CCNE2 mRNA levels (in normalized counts) in purified PBs and the pre-sorting fraction across the cell cycle. Each dot corresponds to one replicate (overlapping replicated appear as 1 dot), with the line connecting the mean value of the replicates. (B) Widefield fluorescence image of synchronized HEK293 cells expressing GFP-LSM14A after smFISH of FBXO5 mRNA. For better visualization, the Cy3 smFISH signal is in green and GFP-LSM14A in red. Nuclei were stained with DAPI (in blue). Individual mRNA molecules appear as small dots (indicated by green arrows). Insets present enlargements of representative PBs, illustrating the heterogeneity of RNA concentration in PBs. Cell cycle phases are indicated on the left. Scale bars, 10 and 1 µm in the images and insets, respectively. (C) Number of FBXO5 mRNA molecules in the cytoplasm or in PBs in individual cells, and resulting fraction of mRNA in PBs across the cell cycle. Each dot corresponds to a cell (n indicated on the x-axis, from 2 independent experiments). Horizontal line, median; error bars, 95% CI. Statistical analyses were performed with a two-tailed Mann-Whitney test: ****, $p<0.0001$; *, $p<0.05$, ns, non-significant ($p>0.5$). (D, E) Same as in B and C, for CLK1 mRNA. (F, G) Same as in B and C, for CCNE2 mRNA.

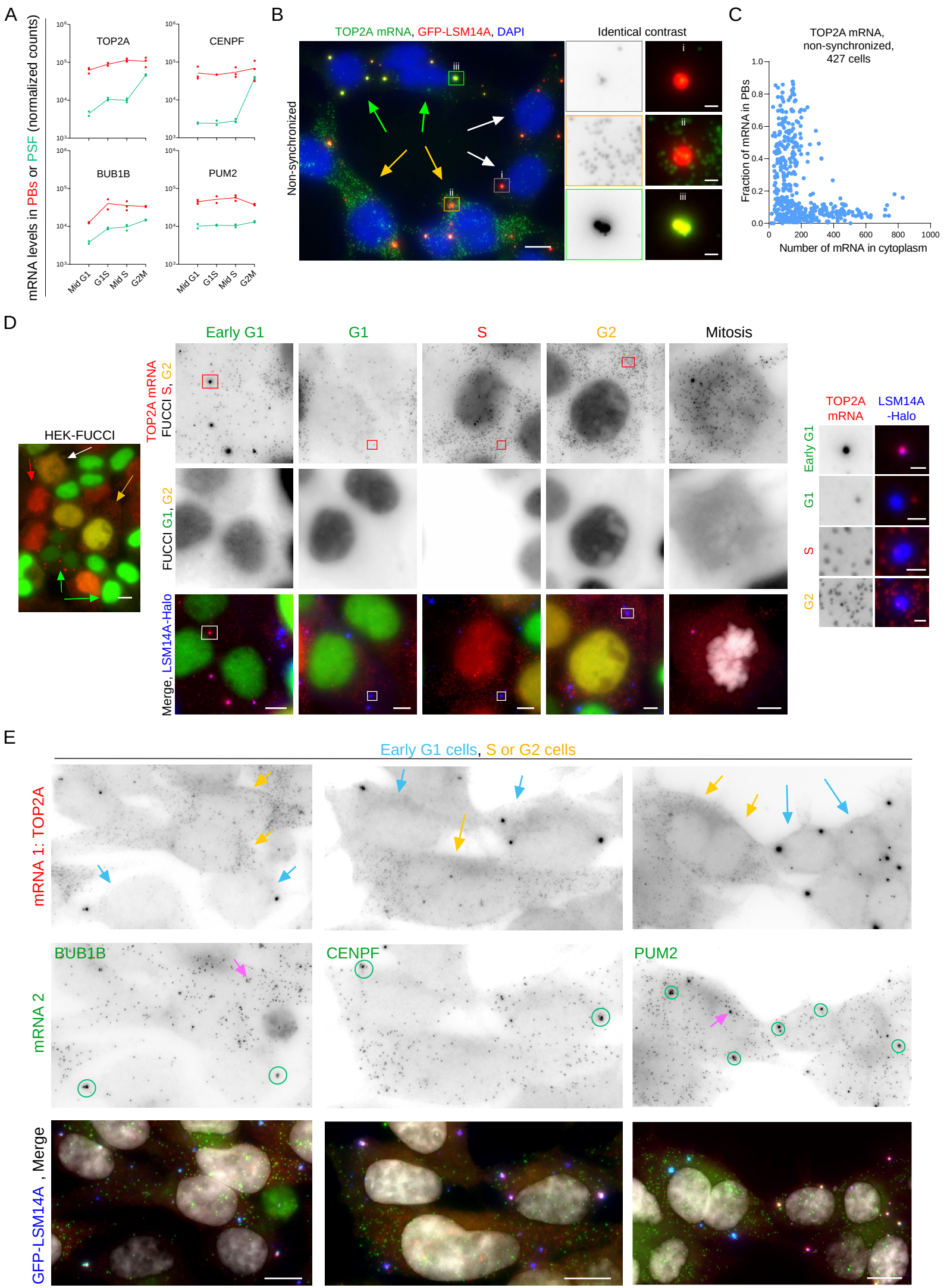
A
mRNA levels in PBs or PSF (normalized counts)
TOP2A
CENPF
BUB1B
PUM2
Mid G1
G1S
Mid S
G2M
B
TOP2A mRNA, GFP-LSM14A, DAPI
Identical contrast
Non-synchronized
C
TOP2A mRNA, non-synchronized, 427 cells
Fraction of mRNA in PBs
Number of mRNA in cytoplasm
D
Early G1
G1
S
G2
Mitosis
HEK-FUCCI
TOP2A mRNA
FUCCI S, G2
FUCCI G1, G2
Merge, LSM14A-Halo
TOP2A mRNA
LSM14A -Halo
Early G1
G1
S
G2
E
Early G1 cells, S or G2 cells
mRNA 1: TOP2A
mRNA 2
BUB1B
CENPF
PUM2
GFP-LSM14A , Merge

**Figure 4: TOP2A, CENPF, BUB1B mRNAs concentrate in PBs after cell division.** (A) Evolution of TOP2A, CENPF, BUB1B, and PUM2 mRNA levels (in normalized counts) in purified PBs and pre-sorting fraction across the cell cycle. Each dot corresponds to one replicate (overlapping replicated appear as 1 dot), with the line connecting the mean value of the replicates. (B) Widefield fluorescence image of asynchronous HEK293 cells expressing GFP-LSM14A after smFISH of TOP2A mRNA. For better visualization, the Cy3 smFISH signal is in green and GFP-LSM14A in red. Nuclei were stained with DAPI (in blue). Insets present enlargements of representative PBs, illustrating the intercellular heterogeneity of RNA concentration in PBs. Green arrows point to cells with low expression and high accumulation in PBs; yellow ones to cells with high expression and low accumulation in PBs; and white ones to cells with low expression and low accumulation in PBs. Scale bars, 10 and 1 µm in the main image and insets, respectively. (C) Fraction of TOP2A mRNAs localized in PBs as a function of their number in the cytoplasm. Each dot corresponds to one cell (n=427, from 2 independent experiments). (D) Left panel: Widefield fluorescence image of HEK-FUCCI cells transiently expressing LSM14A-Halo to label PBs (in far-red, shown in blue), after smFISH of TOP2A mRNA (Cy3, in red). The green, red, yellow, and white arrows point to cells in G1, S, G2, and M, respectively, identified based on the FUCCI system. These cells are enlarged in the middle panels, with the upper row showing the cytoplasmic TOP2A mRNAs and the nuclear mCherry-Gem signal (in red in the merge), the middle row showing the nuclear Cdt1-mVenus (in green in the merge), and the lower row showing the merge including the PB signal (in blue). The mitotic cell was identified based on DAPI staining which is shown in white. Insets on the right present enlargements of the representative PBs framed in white in the merges. Scale bars, 10 µm for left and middle images and 1 µm for insets. (E) 2-color smFISH of TOP2A mRNAs and BUB1B, CENPF or PUM2 mRNAs in asynchronous HEK293 cells expressing GFP-LSM14A. In the merge, TOP2A mRNAs (in Cy5, upper row) are in red, co-detected mRNAs (in Cy3, middle row) are in green, LSM14A-GFP-labelled PBs are in blue, and DAPI-staining of the nuclei in white. Light blue arrows point to early G1 cells and yellow ones to S or G2 cells, as revealed by the TOP2A mRNA labeling pattern. The green circles surround mRNA clustered in PBs. The pink arrows point to nuclear transcription sites. Scale bars, 10 µm.

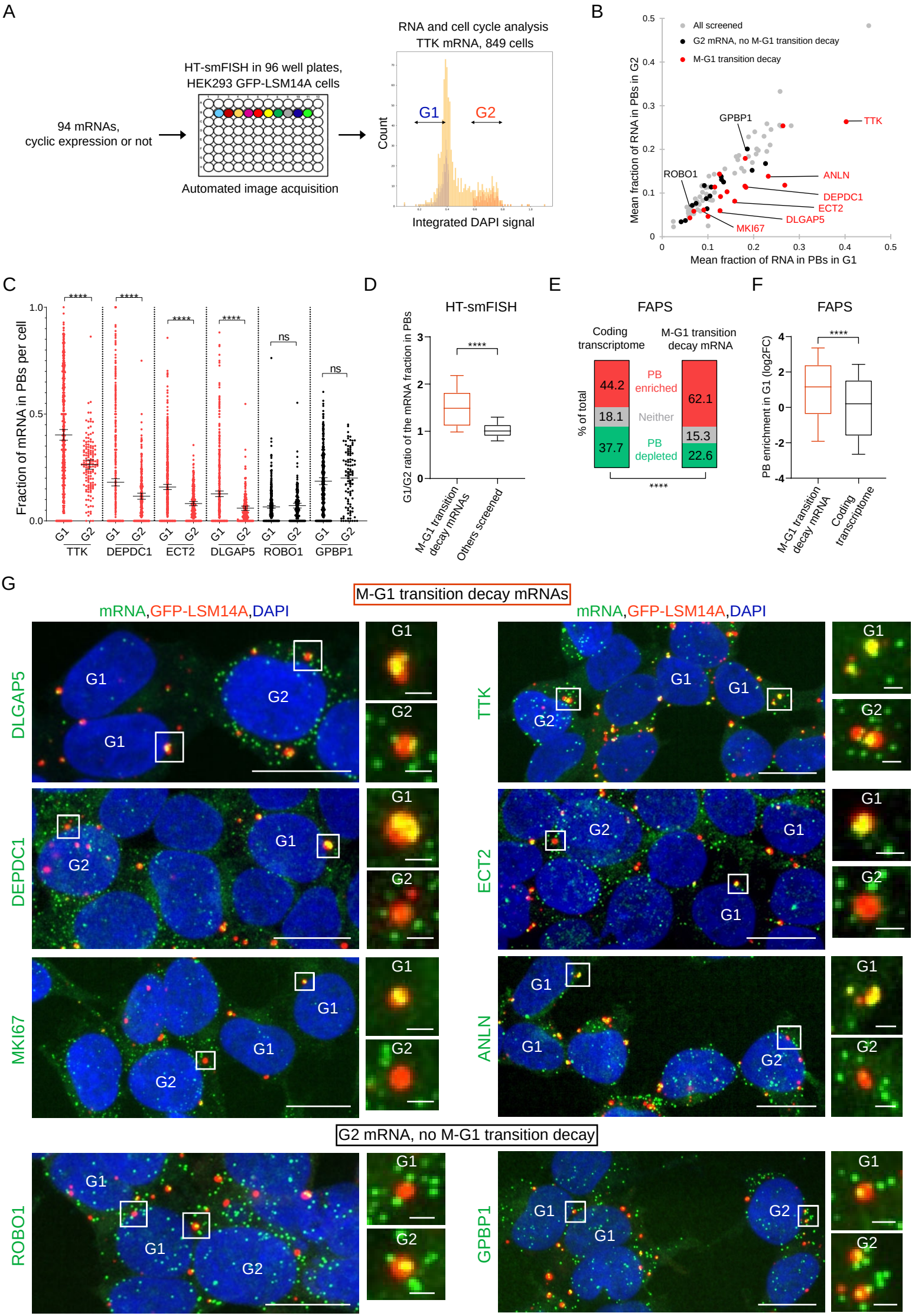
A
94 mRNAs,
cyclic expression or not
HT-smFISH in 96 well plates,
HEK293 GFP-LSM14A cells
Automated image acquisition
RNA and cell cycle analysis
TTK mRNA, 849 cells
G1
G2
Count
Integrated DAPI signal
B
All screened
G2 mRNA, no M-G1 transition decay
M-G1 transition decay
Mean fraction of RNA in PBs in G2
Mean fraction of RNA in PBs in G1
GPBP1
TTK
ROBO1
ANLN
DEPDC1
ECT2
DLGAP5
MKI67
C
Fraction of mRNA in PBs per cell
****
ns
G1
G2
TTK
DEPDC1
ECT2
DLGAP5
ROBO1
GPBP1
D
HT-smFISH
G1/G2 ratio of the mRNA fraction in PBs
M-G1 transition decay mRNAs
Others screened
E
FAPS
Coding transcriptome
M-G1 transition decay mRNA
% of total
44.2
18.1
37.7
62.1
15.3
22.6
PB enriched
Neither
PB depleted
F
FAPS
PB enrichment in G1 (log2FC)
M-G1 transition decay mRNA
Coding transcriptome
G
M-G1 transition decay mRNAs
mRNA,GFP-LSM14A,DAPI
DLGAP5
TTK
DEPDC1
ECT2
MKI67
ANLN
G2 mRNA, no M-G1 transition decay
ROBO1
GPBP1

**Figure 5: A high-throughput smFISH screen reveals PB localization of an mRNA subset after cell division.** (A) Summary of the HT-smFISH workflow and a typical cell cycle profiling based on DAPI staining (taken from TTK mRNA smFISH analysis). The cells considered as in G1 or G2 with good confidence (see material and methods) are indicated in blue and red, respectively. (B) Scatter plot comparing the fraction of mRNA molecules in PBs in G1 and G2 cells for the 94 screened mRNAs. The mRNAs decayed or not during M-G1 transition were taken from Krenning et al., 2022[22]. The named mRNAs are those shown in (G). (C) Dot plot showing the fraction of mRNA molecules in PBs for several transcripts in G1 and G2 cells. The number of analyzed cells for each mRNA ranges from 163 to 837 for G1 cells, and from 54 to 276 for G2 cells, as detailed in Figure S9C. Horizontal line, mean; error bars, 95% CI. Statistical analyses were performed using a two-tailed Welch t test: ****, $p<0.0001$; ns, non-significant ($p>0.5$). (D) Boxplot showing the fold-change of the mRNA fraction in PBs in G1 versus G2 cells for mRNAs decaying at the M-G1 transition and other screened mRNAs. Statistical analyses were performed using a two-tailed Mann-Whitney test: ****, $p<0.0001$. (E) Stacked bar graph showing the proportion of PB-enriched (in red), PB-depleted (in green), or neither (in grey) mRNAs in G1 in the whole coding transcriptome and in the mRNAs decaying at the M-G1 transition (normalized counts >100). Statistical analyses were performed using a Chi-squared test: ****, $p<0.0001$. (F) Box plot showing PB enrichment in G1 for mRNAs decaying at the M-G1 transition and for the whole coding transcriptome (normalized counts >100). Statistical analyses were performed using a two-tailed Mann-Whitney test: ****, $p<0.0001$. (G) Widefield images of HEK293 cells expressing GFP-LSM14A and hybridized using HT-smFISH. Six examples of mRNAs undergoing M-G1 transition decay (upper panels) and 3 examples of mRNAs not undergoing such decay (lower panels) are shown. For better visualization, mRNA is shown in green, PBs in red, and nuclei in blue. DAPI-based cell cycle classification is indicated within cells. Insets highlight differential mRNA accumulation in the PBs framed in white. Scale bars, 10 and 1 µm in the main images and insets, respectively.

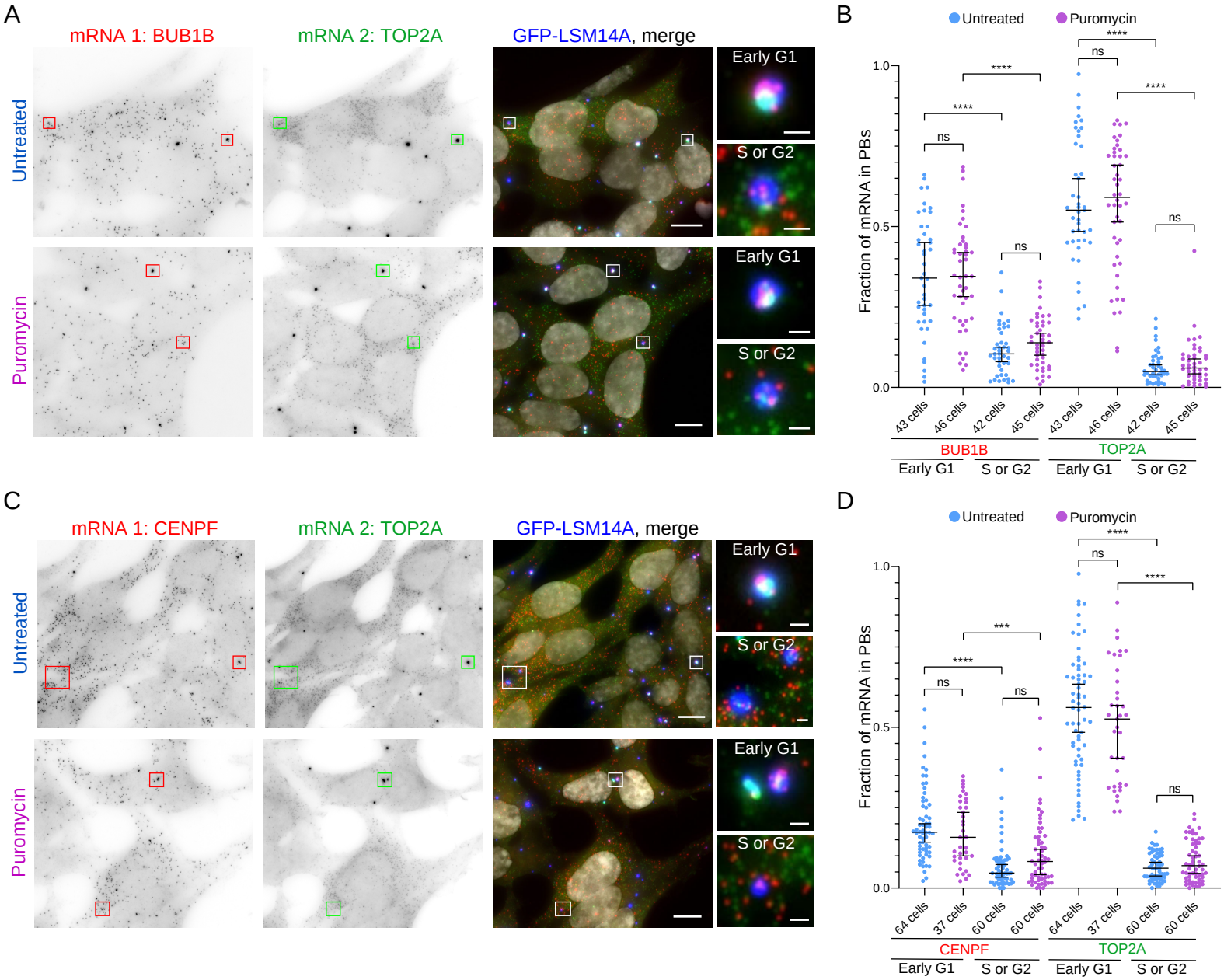
A
mRNA 1: BUB1B
mRNA 2: TOP2A
GFP-LSM14A, merge
Untreated
Puromycin
Early G1
S or G2
B
Untreated
Puromycin
Fraction of mRNA in PBs
1.0
0.5
0.0
****
ns
43 cells
46 cells
42 cells
45 cells
BUB1B
TOP2A
Early G1
S or G2
C
mRNA 1: CENPF
mRNA 2: TOP2A
GFP-LSM14A, merge
Untreated
Puromycin
Early G1
S or G2
D
Untreated
Puromycin
Fraction of mRNA in PBs
1.0
0.5
0.0
***
****
ns
64 cells
37 cells
60 cells
60 cells
CENPF
TOP2A
Early G1
S or G2

**Figure 6: Non-polysomal mRNA levels do not drive cyclic localization of mRNAs in PBs.** (A) 2-color smFISH of BUB1B and TOP2A mRNAs in asynchronous HEK293 cells expressing LSM14A-GFP, treated or not with puromycin for 1 hr. In the merge, BUB1B mRNAs (Cy3, left column) are in red, TOP2A mRNAs (Cy5, middle column) in green, LSM14A-GFP-labelled PBs in blue and DAPI-staining of the nuclei in white. Cells were classified in early G1, or in S or G2 based on TOP2A mRNA labeling pattern. Scale bars, 10 and 1 µm in the main images and insets, respectively. (B) Fraction of BUB1B and TOP2A mRNAs localized in PBs in early G1 and in S or G2, in control and puromycin-treated cells. Each dot corresponds to one cell (n indicated on the x-axis, from 2 independent experiments). Horizontal line, median; error bars, 95% CI. Statistical analyses were performed with a two-tailed Mann-Whitney test: ****, $p<0.0001$; ns, non-significant ($p>0.05$). (C and D) Same as A and B for CENPF and TOP2A mRNAs. ****, $p<0.0001$; ***, $p<0.0005$; ns, non-significant ($p>0.05$).

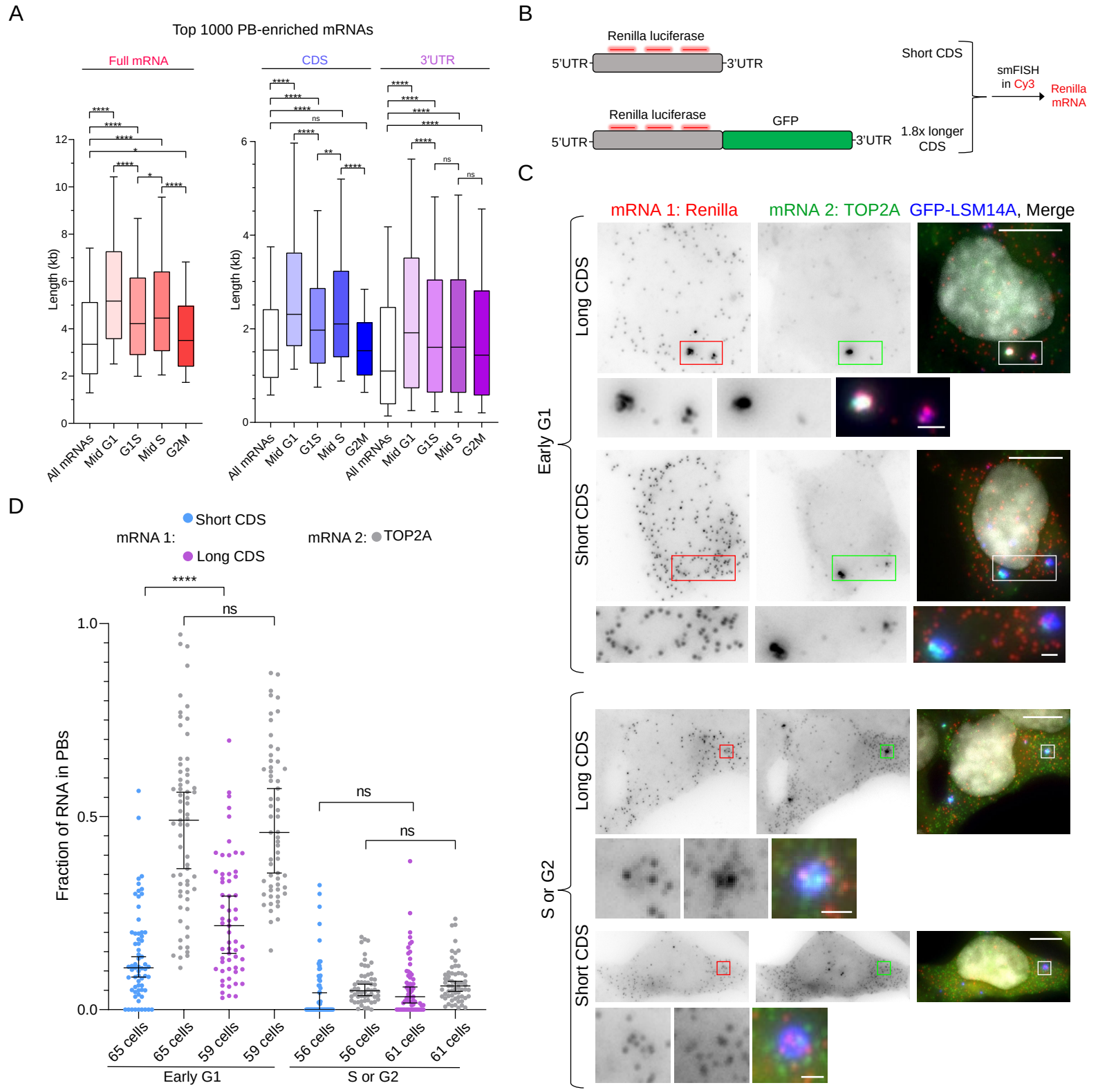
A
Top 1000 PB-enriched mRNAs
Full mRNA
CDS
3'UTR
Length (kb)
All mRNAs
Mid G1
G1S
Mid S
G2M
B
Renilla luciferase
5'UTR
3'UTR
Short CDS
GFP
1.8x longer CDS
smFISH in Cy3
Renilla mRNA
C
mRNA 1: Renilla
mRNA 2: TOP2A
GFP-LSM14A, Merge
Long CDS
Short CDS
Early G1
S or G2
D
Short CDS
mRNA 1:
Long CDS
mRNA 2: TOP2A
Fraction of RNA in PBs
65 cells
65 cells
59 cells
59 cells
56 cells
56 cells
61 cells
61 cells
Early G1
S or G2

**Figure 7: Long CDSs increase RNA accumulation in PBs particularly in early G1.** (A) Lengths of the full mRNA, CDS, and 3'UTR for all detected mRNAs (all mRNAs, normalized counts>100) or for the top 1000 PB-enriched mRNAs (FC>0, p-adj<0.05, cytoplasmic normalized counts>100) in the various cell cycle phases. Whiskers represent the 10 to 90% percentile. Statistical analyses were performed with a two-tailed Mann-Whitney test: ****, p<0.0001; **, p<0.005; *, p<0.05; ns, non-significant (p>0.05). (B) Schematic of the CDS length reporter experiment, with smFISH probes in red. (C) 2-color smFISH of the reporter mRNA and TOP2A mRNA in asynchronous HEK293 cells expressing GFP-LSM14A and transiently transfected with either the long or short form of the Renilla Luciferase reporter. For better visualization, Renilla Luciferase mRNAs (Cy3, left column) are in red, TOP2A mRNAs (Cy5, middle column) in green, GFP-LSM14A-labelled PBs in blue and DAPI in white. Cells in early G1 and in S or G2 were classified based on TOP2A mRNA labeling pattern. Insets below present enlargements of the representative PBs framed in white in the merges. Scale bars, 10 and 1 µm in the main images and insets, respectively. (D) Fraction of long and short Renilla Luciferase mRNAs stored in PBs, with TOP2A mRNAs as an internal control. Each dot corresponds to one cell (n indicated on the x-axis, from 2 independent experiments). Horizontal line, median; error bars, 95% CI. Statistical analyses were performed with a two-tailed Mann-Whitney test: ****, p<0.0001; ns, non-significant (p>0.05).